

ACID-MODIFIED&NICKEL EXCHANGED MORDENITE FOR GAS-PHASE  
HYDRODECHLORINATION OF TRICHLOROETHYLENE

A THESIS SUBMITTED TO  
THE GRADUATE SCHOOL OF NATURAL AND APPLIED SCIENCES  
OF  
MIDDLE EAST TECHNICAL UNIVERSITY

BY

ENES AKYILDIZ

IN PARTIAL FULFILLMENT OF THE REQUIREMENTS  
FOR  
THE DEGREE OF MASTER OF SCIENCE  
IN  
CHEMICAL ENGINEERING

JUNE 2023



Approval of the thesis:

**ACID-MODIFIED&NICKEL EXCHANGED MORDENITE FOR GAS-PHASE HYDRODECHLORINATION OF TRICHLOROETHYLENE**

submitted by **ENES AKYILDIZ** in partial fulfillment of the requirements for the degree of **Master of Science in Chemical Engineering, Middle East Technical University** by,

Prof. Dr. Halil Kalıpçılar  
Dean, Graduate School of **Natural and Applied Sciences**

---

Prof. Dr. Pınar Çalık  
Head of the Department, **Chemical Engineering**

---

Asst. Prof. Dr. Gökhan Çelik  
Supervisor, **Chemical Engineering, METU**

---

Assoc. Prof. Dr. Bahar İpek Torun  
Co-Supervisor, **Chemical Engineering, METU**

---

**Examining Committee Members:**

Prof. Dr. Halil Kalıpçılar  
Chemical Engineering, METU

---

Asst.Prof. Dr. Gökhan Çelik  
Chemical Engineering, METU

---

Assoc. Prof. Dr. Bahar İpek Torun  
Chemical Engineering, METU

---

Prof. Dr. Emrah Özensoy  
Chemistry, Bilkent University

---

Asst.Prof. Dr. Necip Berker Üner  
Chemical Engineering, METU

---

Date: 12.06.2023

**I hereby declare that all information in this document has been obtained and presented in accordance with academic rules and ethical conduct. I also declare that, as required by these rules and conduct, I have fully cited and referenced all material and results that are not original to this work.**

Name Last name : Enes Akyıldız

Signature :

## ABSTRACT

### **ACID-MODIFIED&NICKEL EXCHANGED MORDENITE FOR GAS-PHASE HYDRODECHLORINATION OF TRICHLOROETHYLENE**

Akyıldız, Enes  
Master of Science, Chemical Engineering  
Supervisor: Asst. Prof. Dr. Gökhan Çelik  
Co-Supervisor: Assoc. Prof. Dr. Bahar İpek Torun

June 2023, 78 pages

Contamination of groundwater due to halogenated hydrocarbons is a growing environmental issue because of their abundant utilization in industry and their toxic nature which brings serious concerns about human health. Trichloroethylene (TCE) is one of the frequently observed halogenated compounds in groundwater. Among different water treatment methods, catalytic hydrodechlorination (HDC) effectively removes chlorinated hydrocarbon. Catalytic treatment via HDC is an elimination-based method where the reaction occurs by interacting chlorinated hydrocarbons with hydrogen on a metal catalyst surface, resulting in hydrogen chloride (HCl) and chloride-free hydrocarbons. HDC can be applied on both aqueous and gas phases. The phase of the reaction brings different challenges such as the groundwater matrix effect and proposes different mechanisms and application areas. Numerous studies on different combinations of metals and supports for HDC demonstrate favorable catalytic performance, yet, challenges such as (i) catalyst inhibition due to the reaction product HCl which is irreversibly adsorbed on active sites and causing deactivation, in other words, chloride poisoning, (ii) formation of carbonaceous species on active sites. To adapt catalytic HDC as an elimination-based technique in

the industry these challenges still need to be addressed and improved. Herein this study, the acidity effect of zeolite support material has been tested with dealuminated mordenite (MOR). Since the degree of dealumination directly affects the acidic properties of catalyst support, dealumination was carried out with 6 M and 13 M nitric acid ( $\text{HNO}_3$ ) concentrations, and one sample was left bare without dealumination. Si/Al ratios of HMOR, 6MHMOR, and 13MHMOR are 10, 58, and 101 respectively. Nickel loading to MOR samples was done via ion exchange. Physisorption and crystallographic analysis showed that 3 different acid catalysts remained stable in terms of textural and crystal properties upon harsh-dealumination. The elemental analysis also showed that the percentages of Nickel loadings were similar for all three catalysts. DRIFTS of adsorbed pyridine on dealuminated MORs have shown that number of strong acid sites decreased with respect to the increased degree of dealumination. The activity results of three catalysts showed that the optimized acidity of the catalyst support has a remarkable effect on HDC performance. In terms of percent conversion loss, Ni-6MHMOR presented the best performance with a low amount of carbon and  $\text{Cl}^-$  deposition. Highest carbon formation and  $\text{Cl}^-$  deposition was observed with bare Ni-6MHMOR catalyst during the TGA and TPH analysis.

Keywords: Hydrodechlorination, Trichloroethylene, Nickel, Dealumination, Pyridine DRIFTS, Mordenite

## ÖZ

### ASİT MODİFİKASYONLU VE NİKEL DEĞİŞİMLİ MORDENİTLERLE TRİKLORETİLENİN GAZ FAZINDA HİDRODEKLORİNASYONU

Akyıldız, Enes  
Yüksek Lisans, Kimya Mühendisliği  
Tez Yöneticisi: Dr. Gökhan Çelik  
Ortak Tez Yöneticisi: Doç. Dr. Bahar İpek Torun

Haziran 2023, 78 sayfa

Halojenli içeren hidrokarbonların endüstride sık kullanımları yer altı sularında bu tip hidrokarbonların konsantrasyonlarının artmalarına neden olmaktadır. Bu bileşiklerin toksik yapıları nedeniyle insan sağlığı ve çevreye etkileri büyüyen bir sorun haline gelmektedir. Trikloretilen (TCE), yeraltı sularında sıklıkla gözlenen halojenli bileşiklerden biridir. Farklı su arıtma yöntemleri arasında katalitik hidroklorinasyon (HDC), klorlu hidrokarbonun kimyasal olarak ayrıştırılıp temizlenmesinde etkili bir yaklaşımdır. Katalitik HDC reaksiyonu klorlu hidrokarbonların hidrojen ile metal bir katalizör yüzeyinde etkileşimi ile gerçekleştiği ve hidrojen klorür (HCl) ve klorür içermeyen hidrokarbonlar oluşturduğu eliminasyona dayalı bir yöntemdir. HDC hem sıvı hem de gaz fazında uygulanabilen bir reaksiyondur. İki fazında kendine özgü uygulama alanları, mekanizmaları ve problemleri olabilmektedir. Örneğin sıvı faz uygulamalarında yeraltı sularının matris etkisinden dolayı kataliz deaktivasyonu karşılaşılan farklı problemlerden biridir. yeraltı sularında HDC için farklı metal kombinasyonları ve destekleri üzerine çok sayıda çalışma, olumlu katalitik performans göstermektedir. Ancak (i) aktif bölgelerde geri dönüşümsüz olarak yüzeye tutunan ve dolayısıyla

deaktivasyona neden olan reaksiyon ürünü HCl nedeniyle katalizör inhibisyonu, (ii) aktif bölgelerde karbonlu türlerin oluşumu bu reaksiyonlarda karşılaşılan ana dezavantajlardır. Katalitik HDC yönteminin endüstride eliminasyona dayalı bir teknik olarak kullanılabilmesi için bu dezavantajların ele alınması ve iyileştirilmesi gerekmektedir. Bu çalışmada, zeolit destek malzemesinin katalizör asitliğinin deaktivasyona ve kataliz performansına etkisi dealümine mordenitler (MOR) ile test edilmiştir. Dealüminasyon derecesi diğer bir deyişle konsantrasyonu, katalizör desteğinin asidik özelliklerini doğrudan etkilediğinden, 6 M ve 13 M nitrik asit ( $\text{HNO}_3$ ) konsantrasyonları ile alüminasyon gerçekleştirilmiş ve bir numune, alüminasyon yapılmadan referans olarak bırakılmıştır. HMOR, 6MHMOR ve 13MHMOR'un Si/Al oranları sırasıyla 10, 58 ve 101'dir. MOR numunelerine nikel yüklemesi iyon değişimi ile yapılmıştır. Fiziksel adsorpsiyon ve kristalografik analizler, 3 farklı asit katalizörün şiddetli dealüminasyondan sonra yapısal (gözeneksel) ve kristal özellikleri açısından kararlı kaldığını göstermiştir. Elemental analiz ayrıca nikel yüklemelerinin miktarının her üç katalizör için de benzer olduğunu gösterd. Dealüminasyonlu MOR'lar üzerinde adsorbe edilmiş piridin DRIFTS'leri, dealüminasyonda artan asit yoğunluğuna göre güçlü asit bölgelerinin sayısının azaldığını görüldü. Üç katalizörün aktivite sonuçları, katalizör destek malzemesinin asitliğinin modifiye edilmesi HDC performansı üzerinde dikkate değer bir etkiye sahip olduğunu gösterdi. Dönüşüm kaybı yüzdesi açısından ve en yüksek dönüşüm yüzdesi dikkate alındığında Ni-6MHMOR 3 farklı katalizör arasında en iyi performansı gösterdi. Deaktivasyona sebep olan karbon oluşumu ve  $\text{Cl}^-$  adsorpsiyonu gibi etkenler reaksiyon sonrası analizler ile incelendiğinde ise asiliği değiştirilmemiş Ni-HMOR numunesi en çok karbon oluşumuna ve  $\text{Cl}^-$  tutunumuna sahip olan numune olarak gözlemlendi.

Anahtar Kelimeler: Hidrodeklorinasyon, Trichloroetilen, Nikel, Dealuminasyon, Piridin DRIFTS, Mordenit

To my precious parents, Emine Seher and Mustafa Akyıldız

## ACKNOWLEDGMENTS

I would like to express my profound appreciation and thanks to my advisor Assist. Prof. Gökhan Çelik welcomed me into his research group and offered invaluable direction, and ongoing support throughout my MSc. With his guidance, I have gained many skills that I believe will be essential and instrumental throughout my career and life. I also give my sincere thanks to my co-advisor Assoc. Prof. Bahar İpek Torun for her guidance and invaluable support throughout this journey.

I would like to give my sincere thanks to Laboratory for Advanced Catalysis and Engineering Kinetics (LACEK) family starting from our Post-Docs, Dr. Asmae Bouzini, and Dr. Hamdiye Ece and to my dear colleagues, lab members, and friends Iqtidar Ali Khan, Arzum Ceren Aydoğdu, Uğur Sökmen, and Candan Karaeyvaz for their invaluable support and friendship during my M.Sc. I also would like to thank every member of the Zeolite Synthesis and Application Laboratory for their support and cooperation throughout this way.

Before coming to an end, I would like to deeply thank my dear friend Ali Akman for his priceless support and companionship throughout this way. I also heartedly thank my dear friends İrem Giray, Nuri Eryılmaz, and Sinan Okunakol for their invaluable friendship and support during my M.Sc.

Last but not least one of course goes to my precious family. My deepest gratitude always goes to my parents Seher and Mustafa for their unconditional love and support throughout my life. I would also like to thank my lovely sister Firdevs and dear big brothers Halil İbrahim and Zahid for their priceless love and support. Finally, I should thank my dear extended family.

This study was funded partly by TUBİTAK BİDEB 118C260 and fully by BAP AGEF-304-2023-11302 projects. METU Central Lab, UNAM, BUMER,

DAYTAM, and METU Chemical Engineering Department Facilities were used for characterization.

## TABLE OF CONTENTS

ABSTRACT .....	v
ÖZ.....	vii
ACKNOWLEDGMENTS .....	x
TABLE OF CONTENTS .....	xii
LIST OF TABLES .....	xv
LIST OF FIGURES .....	xvi
LIST OF ABBREVIATIONS .....	xix
CHAPTERS	
1 INTRODUCTION .....	1
1.1 TCE as Environmental Pollutant .....	1
1.2 Common Remediation Technologies of TCE .....	3
1.3 Catalytic Hydrodechlorination of Trichloroethylene .....	5
1.4 Zeolites .....	9
2 LITERATURE REVIEW .....	13
3 EXPERIMENTAL PROCEDURES .....	17
3.1 Chemicals and Materials .....	17
3.2 Catalyst Preparation.....	17
3.2.1 Dealumination of the Mordenite Support .....	17
3.2.2 Ni Incorporation via Ion-Exchange .....	18
3.3 Characterization Experiments .....	19
3.3.1 Inductively Coupled Plasma – Optical Emission Spectroscopy (ICP-OES) .....	19

3.3.2	N <sub>2</sub> Physisorption Experiments .....	19
3.3.3	Temperature Programmed Reduction under H <sub>2</sub> (H <sub>2</sub> -TPR).....	20
3.3.4	Post Reaction Temperature Programmed Hydrogenation (TPH) .....	20
3.3.5	CO Pulse Chemisorption .....	21
3.3.6	X-Ray Diffraction Analysis (XRD) .....	21
3.3.7	X-Ray Photoelectron Spectroscopy (XPS) .....	21
3.3.8	In-Situ Diffuse Reflectance Infrared Fourier Transform Spectroscopy (DRIFTS) of Adsorbed Pyridine.....	22
3.3.9	Thermogravimetric Analysis (TGA) of Spent Catalysts.....	22
3.3.10	High-Resolution Transmission Electron Microscopy (HR-TEM) sample preparation .....	22
3.4	Catalytic HDC Activity Tests .....	24
4	RESULTS AND DISCUSSIONS.....	27
4.1	Dealumination of Mordenite Support .....	27
4.1.1	N <sub>2</sub> physisorption Results of XM-HMORs and Ni-XM-HMORs .....	27
4.1.2	X-Ray Diffraction Results of BAMORs .....	29
4.1.3	DRIFTS of Adsorbed Pyridine Results over Dealuminated MORs.....	31
4.2	Ni loading to XM-HMORs via Ion Exchange .....	34
4.2.1	ICP-OES Results .....	34
4.2.2	H <sub>2</sub> -Temperature Programmed Reduction Results .....	37
4.2.3	Nickel Particle Size Analysis by HR-TEM.....	39
4.3	Results of Gas-phase HDC of TCE .....	45
4.4	Post-Reaction Analysis of Used Catalysts .....	52
4.4.1	Thermogravimetric Analysis of Used Catalysis.....	52

4.4.2	Temperature Programmed Hydrogenation of Used Catalysts .....	53
5	CONCLUSIONS .....	57
	REFERENCES .....	59
APPENDICES		
A.	Calculations of Catalytic Activity Parameters .....	73
B.	Result of CO pulse chemisorption on Ni-HMOR .....	75
C.	XPS Results of HDC Used Ni-HMOR catalyst .....	76

## LIST OF TABLES

### TABLES

Table 1. Textural properties and elemental analysis of bare and dealuminated MORs. .....	29
Table 2. Crystal sizes of bare and dealuminated MORs,.....	31
Table 3. Peak assignments for bare and dealuminated MORs over pyridine DRIFTS. .....	33
Table 4. Elemental analysis of Ni exchanged HMORs dealuminated to a different extent.....	36
Table 5. Textural properties of Ni exchanged XMHMORs.....	36
Table 6. Tabulated HDC activity results of Ni exchanged XMHMORs at 300 °C, 1 atm and H <sub>2</sub> :TCE~60:1.....	48
Table 7. Tabulated product distributions over Ni exchanged XMHMORs at 300 °C, 1 atm and H <sub>2</sub> :TCE~60:1.....	49

## LIST OF FIGURES

### FIGURES

Figure 1. Chemical Structure of Trichloroethylene (TCE).....	2
Figure 2. Basic classification and examples of current remediation technologies for chlorinated organic compounds [2] Reused with permission. Copyright 2014, Elsevier, Environment International.....	3
Figure 3. Example of the proposed reaction mechanism based on adsorption for HDC of TCE over Pd nanoparticle catalyst [27]. Reused with permission. Copyright 2014, John Wiley and Sons, Journal of Chemical Technology & Biotechnology.....	6
Figure 4. Illustration of the application of air sparging technology for contaminated groundwater sites [35]. Reused with permission. Copyright 2004, Elsevier, Environmental Monitoring and Characterization.....	8
Figure 5. Examples of some subunits, cages, and cavities recurring in different frameworks [40]. .....	9
Figure 6. The MOR framework type (a) its' projection along [001] plane, (b) channel connection block, (c) 12-MR channel along c, and (d) 8-MR channel along c (retrieved from <a href="http://www.iza-online.org">http://www.iza-online.org</a> ).....	10
Figure 7. Scheme of different paths to obtain hierarchical zeolites [41]. Permission is not required for non-commercial use.....	11
Figure 8. Experimental scheme for dealumination of HMORs.....	18
Figure 9. Schematic of nickel exchange procedure for XMHMORs .....	19
Figure 10. Experimental set-up for aqueous phase HDC tests.....	24
Figure 11. Flow Diagram of gas phase HDC activity system .....	25
Figure 12. Picture of HDC activity system and its major components in series with in-situ DRIFTS system .....	26
Figure 13. (a) Nitrogen adsorption-desorption isotherms, Inset: hysteresis, and (b) BJH adsorption pore-size distribution of bare and dealuminated MORs.....	28
Figure 14. X-Ray diffraction patterns of untreated and dealuminated MORs. ....	30

Figure 15. DRIFTS spectra of adsorbed pyridine over (a) HMOR, (b) 6MHMOR, and (c) 13MHMOR from 50 °C to 450 °C. ....	34
Figure 16. Dealumination acid concentration vs. obtained Si/Al ratio plot.....	35
Figure 17. (a)Nitrogen adsorption-desorption isotherms, Inset: hysteresis, and (b) BJH adsorption pore-size distribution of bare and dealuminated Ni exchanged MORs.....	37
Figure 18. H <sub>2</sub> -TPR profiles of the bare and dealuminated Ni-loaded HMORs.....	39
Figure 19. High Resolution TEM images and particle size distributions of (a) Ni-HMOR, (b) Ni-6MHMOR, and (c) Ni-13MHMOR.....	41
Figure 20. Cl <sup>-</sup> concentration within the reactor with respect to time during the HDC of TCE with Ni-HMOR catalyst. ....	43
Figure 21. HPLC results of HDC with Pd/Al <sub>2</sub> O <sub>3</sub> catalyst. ....	44
Figure 22. HPLC results of HDC with Ni-HMOR catalyst. ....	45
Figure 23. TCE conversion of Ni exchanged XMHMORs with respect to time at 300 °C, 1 atm and H <sub>2</sub> :TCE~60:1. ....	48
Figure 24. TCE conversion of bare Ni-HMORs with respect to time at 300 °C, 1 atm and H <sub>2</sub> :TCE~60:1 with different pre-reduction times.....	49
Figure 25. Product selectivity distributions with respect to time of 3 different catalysts a) Ni-HMOR b) Ni-6MHMOR and c) Ni-13MHMOR at 300 °C, 1 atm and H <sub>2</sub> :TCE~60:1. ....	50
Figure 26. TCE conversion of Ni exchanged XMHMORs with respect to time at 300 °C, 1 atm with H <sub>2</sub> :TCE~13. ....	51
Figure 27. Selectivity product distributions with respect to time of 3 different catalysts a) Ni-HMOR b) Ni-6MHMOR and c) Ni-13MHMOR at 300 °C, 1 atm and H <sub>2</sub> :TCE~13.....	51
Figure 28. Background activity of HMOR (bare) and 6MHMOR (dealuminated) supports at 300 °C, 1 atm and H <sub>2</sub> :TCE~60:1.....	52
Figure 29. TGA results of HDC-tested Ni-XMHMORs, 300°C, 1 atm and H <sub>2</sub> :TCE~60:1. ....	53

Figure 30. TPH of used catalysts, represents (a) the $m/z=36$ signal of HCl , (b) the $m/z=16$ signal of CH <sub>4</sub> and (c) the $m/z=38$ signal with respect to increasing temperature. ....	55
Figure 31. $m/z=28$ signal collected for 6 CO pulses on the Ni-HMOR sample.....	75
Figure 32. $m/z=28$ signal collected for 6 CO pulses on the Pt/TiO <sub>2</sub> sample.....	75
Figure 33 Elemental XPS results of HDC used Ni -HMOR catalyst. ....	76
Figure 34. Deconvoluted XPS plots for Cl, Al, and C elements on HDC used Ni-HMOR catalyst. ....	77
Figure 35. XRD patterns obtained for Ni exchanged bare and dealuminated MORs. ....	78

## LIST OF ABBREVIATIONS

### ABBREVIATIONS

XRD	X-Ray Diffraction
HR-TEM	High Resolution Transmission Electron Microscopy
ICP-OES	Inductively Coupled Plasma-Optical Emission Spectrometer
DRIFTS	Diffuse Reflectance Infrared Fourier Transform Spectroscopy
TGA	Thermogravimetric Analysis
TPR	Temperature Programmed Reduction
TPH	Temperature Programmed Hydrogenation
TPD	Temperature Programmed Desorption
XPS	X-Ray Photoelectron Spectroscopy
BET	Brunauer–Emmett–Teller
BJH	Barrett-Joyner-Halenda
FID	Flame Ionization Detector
GC	Gas Chromatography
GHSV	Gas Hourly Space Velocity
TCE	Trichloroethylene
HDC	Hydrodechlorination
VOCs	Volatile Organic Compounds
CHs	Chlorinated Hydrocarbons
EPA	Environmental Protection Agency
WHO	World Health Organization



# CHAPTER 1

## INTRODUCTION

### 1.1 TCE as Environmental Pollutant

Due to the extensive use of groundwater as drinking water and its possible consequences on the ecosystem, groundwater pollution by harmful volatile organic compounds (VOCs) has become a major public concern in recent years. Chlorinated hydrocarbons (CHs) are one of the VOCs most frequently discovered in aquatic habitats, according to environmental assessment studies [1]. All around the world, groundwater is utilized as a clean and fresh water source for drinking water, industrial and agricultural applications. Due to its' vital usage areas contamination of groundwater brought serious concerns to public health and the environment.

The main issue is the widespread use of commercial CHs as solvents, cleaning agents, and extracting agents in the pharmaceutical, chemical, electronic, and heavy metal industries [1], [2]. Trichloroethylene also known as trichloroethene (TCE), a chlorinated hydrocarbon with the chemical formula  $C_2HCl_3$ , is frequently detected in groundwater compared to other chlorinated pollutants because of its considerably higher solubility [3]. TCE is a non-flammable colorless liquid with a sweet smell. It has a chemical structure as shown in Figure 1. TCE, an efficient organic solvent, is frequently used as an industrial solvent to remove grease from a variety of surfaces and materials, particularly in the metal sector. Due to TCE's highly volatile nature, exposure to TCE from the air is also highly possible [4]. It is even utilized in many daily life consumer products and its emission to the atmosphere and human exposure was strictly not recommended by some assessment studies [5]. TCE was shown to be as highly toxic, carcinogenic, and hazardous [2], [4]–[6]. TCE has been reported to have detrimental effects on the immune system, nervous system, and hormonal system in adults [7], [8]. It is also thought to cause kidney, liver, multiple myeloma,

pediatric leukemia, and so on [9], [10]. TCE was ranked as the 16th most hazardous chemical on the Agency for Toxic Substances and Disease Registry's list of National Priorities [11], [12].

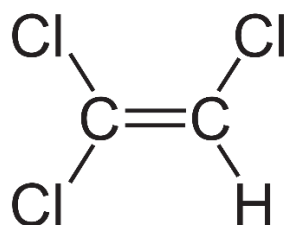


Figure 1. Chemical Structure of Trichloroethylene (TCE)

TCE contamination results from inappropriate process water disposal and difficult chemical handling since TCE has high vaporization affinity and high values of Henry's constant. Different studies addressed one of the major sources of TCE leakage is chemical handling of TCE [4], [13]. During both its' use and manufacturing, TCE is discharged into the environment. The primary sources of contamination are industrial charges, wastes, and improper disposal of process water from metal degreasing plants.

Regulations are very rigorous when it comes to TCE management. There are strict regulations regarding TCE concentrations in groundwater. For example, the Environmental Protection Agency (EPA) limits the maximum TCE concentration to 5 ppb and it has a target of 0 ppb contamination level for groundwater in the USA [8], [12]. Unfortunately, depending on the degree and nature of the contamination, TCE concentrations in drinking water can exceed 49 mg/l and in groundwater can reach 950 mg/l [14]. TCE production was approximated at 145,000 tonnes per year in the U.S. in 1991 whereas 131,000 tonnes in Europe in 1990 [2], [15]. China's TCE production was reported as 250,000 tonnes in 2011 and demand for TCE was assessed to be increased every year [2]. These growing production numbers justify the increasing concerns regarding public health and the environment.

## 1.2 Common Remediation Technologies of TCE

There are different techniques to remove chlorinated organic compounds including TCE from contaminated media. These techniques are divided into two main branches: elimination-based (destructive) techniques and recovery-based (non-destructive) techniques as is seen in Figure 2. As the name implies elimination-based techniques eliminate the chlorinated contaminant by converting it to less-harmful benign compounds within a single step without requiring further treatments [16]–[18]. On the other hand, recovery-based methods impose recovery via transferring of contaminant from one media to another in which further processes are required for complete remediation.

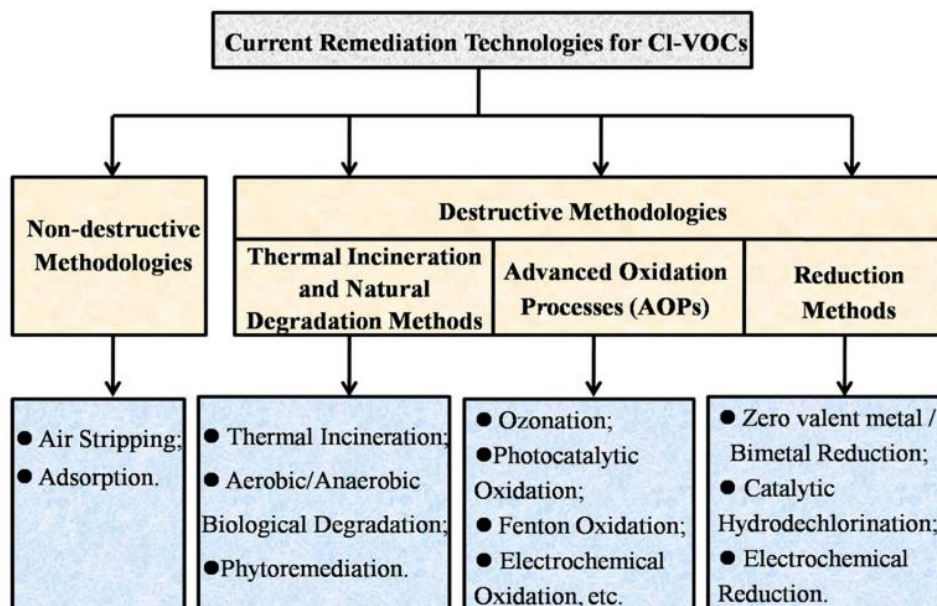


Figure 2. Basic classification and examples of current remediation technologies for chlorinated organic compounds [2] Reused with permission. Copyright 2014, Elsevier, Environment International.

On the other hand, hydrodechlorination (HDC) is an elimination-based method where the chlorinated contaminant is completely decomposed into harmless compounds. Complete HDC reaction takes place by conversion of hydrogen and TCE to ethane and hydrogen chloride HCl via catalytic pathway at respectively low

temperatures or without a catalyst at high temperatures. The reaction equation is generally the same for all chlorinated hydrocarbons in which the end products are dechlorinated hydrocarbons and hydrogen chloride upon complete HDC [19]

Activated carbon adsorption and air stripping are two frequently utilized recovery-based remediation techniques. Air stripping involves flushing chlorinated chemicals out of groundwater using a flow of hot air. Although TCE may create a dense bottom layer at high concentrations, which is difficult to remove with air stripping, its high tendency to evaporate makes air stripping practical [16], [20]. Hazardous compounds are adsorbed using the activated carbon technique, and then they are desorption-transferred to another media where the contaminant-containing stream needs to be further treated [21]. Air stripping methods require highly powered and costly pumping-heating systems and infrastructure whereas regeneration of old adsorbents and replacement of the adsorbent are the limitations of these two methods respectively [16].

Biological degradation of chlorinated contaminants from water is another destructive method where the complete reduction of contaminant is done by special enzymes within microorganisms. Even if this method can achieve complete degradation under mild natural conditions, it is inefficient in terms of time due to slow reaction kinetics [2], [16], [20]. Thermal incineration and oxidation techniques such as ozonation, electrochemical oxidation, etc. are also destructive process in which contaminant is combusted or converted in the oxygenating environment to chloride-free contaminants. However certain drawbacks like the addition of expensive chemicals, undesirable by-products from the unselective oxidation of chlorinated contaminants by radical intermediates, and significant energy consumption must be rendered for future applications [2], [20].

The TCE removal techniques commonly available for groundwater are adsorption, extraction, air stripping, incineration via oxidation, and bioremediation. These methods have certain drawbacks such as time inefficiency, demanding further treatments and excess energy, and the possibility to have more toxic compounds [16],

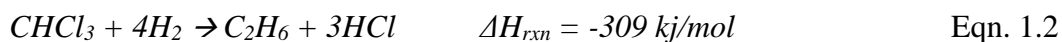
[20]–[22]. Electrochemical reduction is another technique similar to catalytic HDC in terms of mechanism which is done under an electric field. This technique is also promising in terms of reduction performance however a larger design for industrial applications is still a challenge [2]. Zerovalent iron reduction is another common technique giving reasonable performances under atmospheric conditions. However, several technical difficulties, including bed positioning and active phase leaching, make it still a slower procedure than HDC [23], [24].

The certain limitations of current recovery methods and reductive methods drive the motivation towards research on catalytic HDC reduction. HDC is applicable with certain transition metal catalysts both in atmospheric and mildly elevated temperatures depending on the metal [19], [25]. It is possible to apply gas-phase catalytic HDC on-site applications where contaminants are released into the atmosphere or water with high concentrations. TCE vapors from big plants that typically use chemical or incinerator oxidation processes can be treated using gas phase HDC of TCE [26]. Switching from batch to continuous operation is also significant considering that economies of scale support continuous processes for high throughput.

### **1.3 Catalytic Hydrodechlorination of Trichloroethylene**

Catalytic hydrodechlorination of chlorinated hydrocarbons occurs via the elimination of contaminants in the presence of hydrogen and catalyst. Chlorinated contaminants react with hydrogen and transform into hydrogen chloride and chloride-free hydrocarbons. The overall desired reaction equation is given in Equation 1.1. A represents the hydrocarbon chain of chlorinated compounds [19]. Ideally, the completed HDC of the TCE reaction can be written as in Equation 1.2. The reaction mechanism for hydrodechlorination generally follows the sequential dechlorination of chlorine atoms via a hydrogenated metal catalyst [19]. Of course, the detailed reaction mechanisms may vary depending on the chlorinated molecule, catalyst, and reaction conditions. Figure 3 represents one of the reaction mechanisms

proposed for the HDC of TCE over Pd nanoparticles in the aqueous and atmospheric environment [27].



In comparison to common remediation techniques, catalytic reduction of chlorinated chemicals using HDC has several benefits. First of all, a variety of chlorinated substances, including hydrocarbons, chlorophenols, and polycyclic aromatic (PAHs) chemicals, can be hydrodechlorinated successfully over metal-supported heterogeneous catalysts, at low and mildly high-temperature ranges. HDC's has relatively fast kinetics at room temperature without the requirement for high temperatures as in the oxidation techniques and thermal degradation. Moreover, HDC does not possess more toxic compounds such as  $Cl_2$  and dioxins produced in combustion or incineration techniques. The reductive nature of HDC also provides no  $SO_x$  and  $NO_x$  gases that could be formed upon wet oxidation, and biological and photocatalytic eliminations [28].

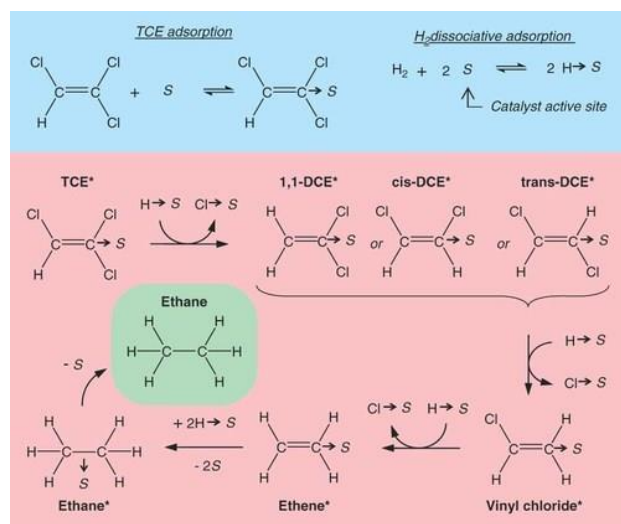


Figure 3. Example of the proposed reaction mechanism based on adsorption for HDC of TCE over Pd nanoparticle catalyst [27]. Reused with permission. Copyright 2014, John Wiley and Sons, Journal of Chemical Technology & Biotechnology.

Different reaction conditions have been tested for HDC with a wide variety of catalysts so far. HDC reactions have been mostly conducted in the aqueous phase and gas phase. There were also organic phase and organic-aqueous mixture studies conducted [29]–[31] to understand the reaction mechanisms by lowering the major deactivation constraints raised upon reaction products and the environment. Precious metals like Pt and Pd can give high activities in aqueous environments even at room temperature and atmospheric pressures whereas Ni-based metal catalysts start to give considerable activities at mildly elevated temperatures and atmospheric pressures [19], [25]. High-pressure aqueous phase reactions have also been tested for HDC of chlorinated hydrocarbons up to 50 bar by different authors in batch and continuous flow reactors [24], [25], [29], [32]–[34].

Aqueous phase studies are more common compared to continuous gas phase applications in the literature. Considering direct field applications, aqueous phase HDC is more reasonable since the reaction can occur at room temperature and atmospheric conditions without a need for high energy inputs. However, aqueous phase applications have also certain challenges. The first one is the limited hydrogen solubility in water in atmospheric conditions can limit the reaction. At atmospheric conditions, 293 K 101.3 kPa, H<sub>2</sub> solubility in water is approximately 0.8 mM. The second reason is water itself brings some additional deactivation mechanisms like metal leaching due to the reaction product of HCl and catalyst poisoning due to compounds like SO<sub>4</sub><sup>2-</sup>, SO<sub>3</sub><sup>2-</sup>, HS<sup>-</sup>, NO<sub>3</sub><sup>-</sup>, NO<sub>2</sub><sup>-</sup> etc. readily found in groundwater sources [23]. This is also known as the groundwater matrix effect on catalyst activation [29].

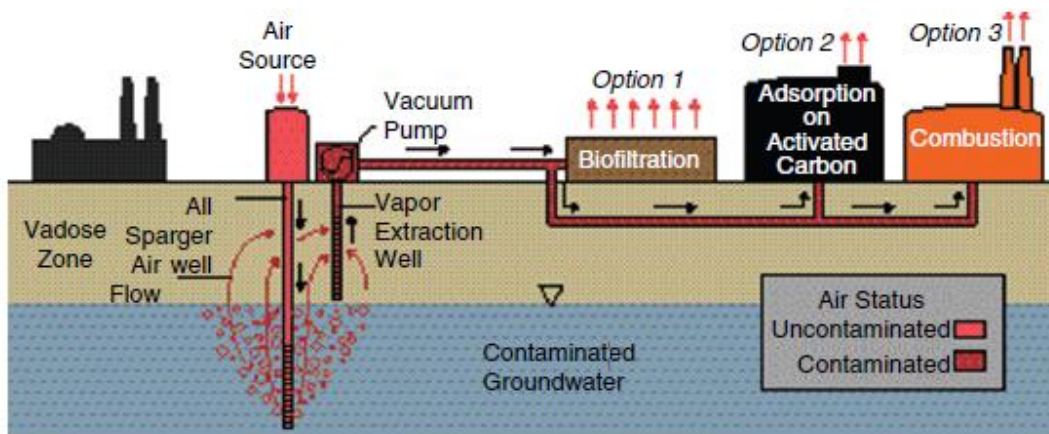


Figure 4. Illustration of the application of air sparging technology for contaminated groundwater sites [35]. Reused with permission. Copyright 2004, Elsevier, Environmental Monitoring and Characterization.

Gas phase HDC of chlorinate compounds has also been carried out in many studies [19], [25], [36]–[39]. Gas phase applications can be utilized for direct elimination with on-site applications where the target contaminant is released to the atmosphere and environment or incinerated through oxidative techniques. The second alternative for applicational usage of gas phase HDC can be done via air sparging using secondary units to transfer expected contaminants as is seen in Figure 4. In this technique, air is bubbled through the ground water source and vacuumed through the pump to remediation sites which can be biofiltration, adsorption or combustion units, or combination of some or all of these units with HDC. Gas phase HDC reactions also suffer from deactivation due to chloride species. The sources of chloride can come from the reaction product itself  $\text{Cl}^-$  or dissolved  $\text{Cl}^-$  due to the  $\text{HCl}$  formation. The dissolution effect is more likely to occur in the aqueous phase HDC than the gas phase. Deactivation due to the matrix effect will be diminished through gas phase applications since the transferring of poisoning ions via sparging would be excessively low and considering the direct on-site elimination these ions will no longer be a consideration.

## 1.4 Zeolites

Zeolites are crystalline, nano-porous aluminosilicates with the tetrahedral corner-sharing of  $\text{SiO}_{4/2}$  and  $\text{AlO}_{4/2}$ . Zeolites are generally classified according to their framework type. The framework of zeolites is determined by the cages and channels they are formed with different pore sizes in the range of 0.3 to 2nm. The chemical formula of zeolites is in the form of  $\text{M}^{n+}_{x/n}[(\text{SiO}_2)_y(\text{AlO}_2)_{-x}] \cdot m\text{H}_2\text{O}$ . Negative charge of  $[\text{AlO}_{4/2}]^-$  is in balance with the cation which can be alkali metal, alkaline earth metal or transition metal cation [40]. All zeolite or zeolite-like materials share a 3-dimensional, 4-connected framework structure made of corner-sharing  $\text{TO}_4$  tetrahedra (basic building unit, or BBU), where T is any tetrahedrally coordinated cation. Figure 5 represents some of the basic recurring building blocks in different types of zeolites.

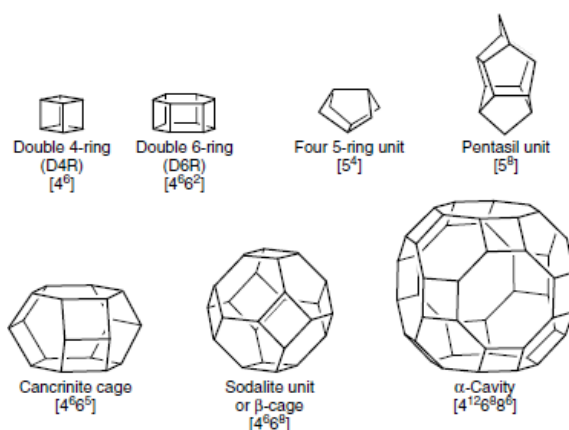


Figure 5. Examples of some subunits, cages, and cavities recurring in different frameworks [40].

The first thing that describes zeolites is their framework type including the size of pore openings and dimensions of their channel systems. These types are generally formed upon specific alignment, recurrence, and positioning of their subunit and basic building. The most common and industrially synthesized framework types are Sodalite (SOD), Linde Type A (LTA), Faujasite (FAU), Chabazite (CHA), ZSM-5 (MFI), Mordenite (MOR), Zeolite beta (BEA) and so on. Herein this study, MOR type of zeolite has been studied. MOR has 4 four 5 rings joined together with

common edges and they form chains in this way as it is seen in the as in Figure 6a. These sheets are connected via oxygen bridges to corrugated sheets which are then connected to finally form 12-member ring and 8-member ring channels. The transition between the channels is generally limited due to the structural formation of the channels. Thus, the MOR type of zeolite generally allows 1-D effective diffusion throughout its' channels. Depending on the size of the reactant or adsorbent, the process may only occur through the 12-MR pore channeling since other channel openings are considerably smaller than the 12-MR pore opening.

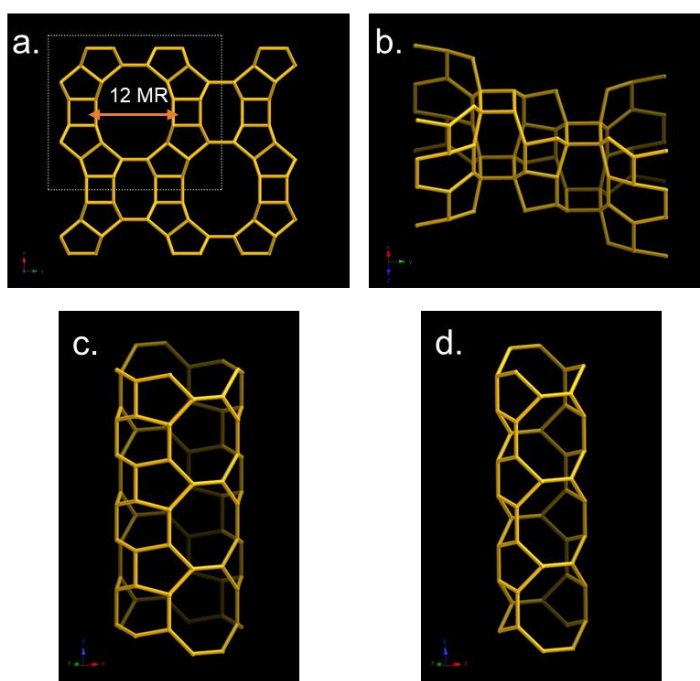


Figure 6. The MOR framework type (a) its' projection along [001] plane, (b) channel connection block, (c) 12-MR channel along c, and (d) 8-MR channel along c (retrieved from <http://www.iza-online.org>).

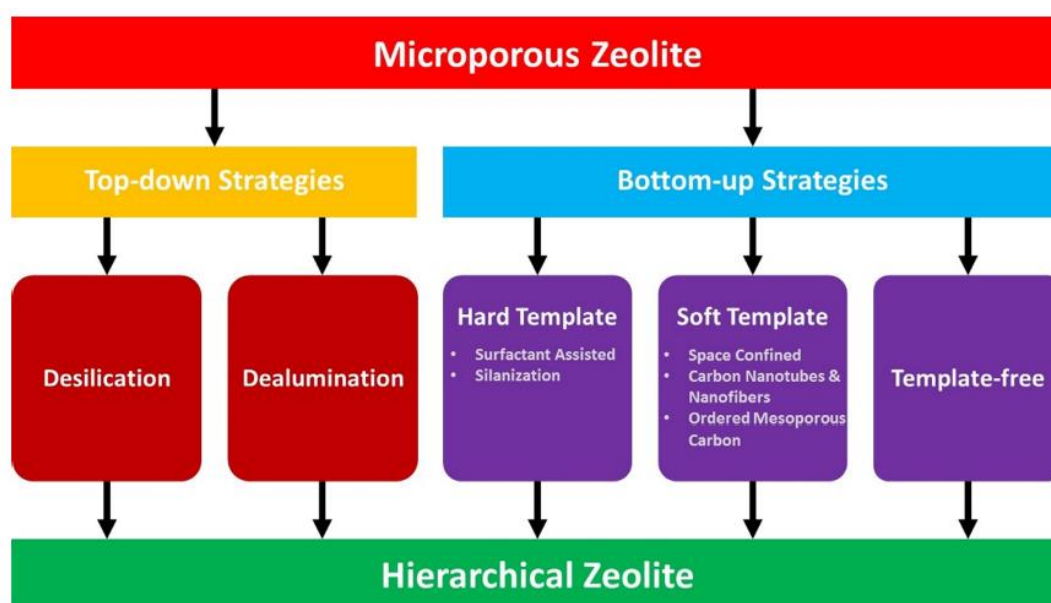


Figure 7. Scheme of different paths to obtain hierarchical zeolites [41]. Permission is not required for non-commercial use.

Zeolites also known as molecular sieves' porous features make them useful as adsorbents. Zeolites are used in catalytic applications as well because of their excellent thermal and hydrothermal stability, strong acid sites, and ion exchange capabilities. 13% of the zeolites produced in the world are used for catalysis [40]. Particularly in hydrocracking and catalytic cracking processes, zeolites are used as heterogeneous catalysts. However, they have some drawbacks such as (i) when the reactants have dimensions that are similar to or greater than the micropores, diffusion can be restrained due to the inaccessible active sites, (ii) unwanted side products that blocks micropores and render the catalyst inactive. To overcome these limitations, larger pore-sized zeolites or hierarchical zeolites are synthesized by different methods. Figure 7 represents the most commonly known top-down and bottom-up strategies utilized for the synthesis of hierarchical zeolites. Dealumination is mostly carried out by acid treatments such as nitric acid, hydrochloric acid, oxalic acid, and so on [41], [42]. Desilication is mostly done by steam treatment or base treatments with NaOH. There is also a dissolution and recrystallization procedure among top-down strategies in which zeolite is completely dissolved to the smallest components to be recrystallized with differently ordered hierarchical structures [42]. In the scope

of this study, the dealumination strategy is followed due to ease of applicability and effectiveness for dealuminating the commercially available or already synthesized zeolite structure. One other parameter is to modify zeolite acidity by extracting the Al atoms from the zeolite structure since Al atoms are known for their contribution to the acidity of zeolite.

## CHAPTER 2

### LITERATURE REVIEW

HDC is an elimination-based remediation method where the chlorinated contaminant is catalytically converted to benign compounds over a metal surface [19]. To date, many studies have been conducted on the HDC of chlorinated hydrocarbons utilizing supported metals, metal nanoparticles, and reductive agents like zerovalent iron (ZVI) [31], [43]–[45]. Palladium-based catalysts have been vastly studied by different authors for HDC since noble metals like Pt, and Pd work as efficient hydrogenation catalysts considering the performance of the catalyst giving almost 100% conversions in HDC reaction in mild conditions with different chlorinated contaminants [22]. HDC of chlorinated ethenes has been tried on supported and unsupported (nanoparticles) metals including Pd, Pt, Rh, Ru, Ni, Mo, and V over various supports including alumina, silica, and carbon [43], [46]–[53]. Since noble metals give high activity towards HDC, recent studies generally focus on preventing the deactivation of Pd metal due to HCl formation during the reaction. Sohn et al. and Celik et al. utilized swellable organically modified silica (SOMS) material as a support for Pd metal to promote its catalytic properties and it prevents poisoning and leaching effects caused by HCl during HDC of TCE because of its swelling nature [26], [31]–[33], [54]. Ordonez et al. also studied the effect of the HCl leaching and Cl<sup>-</sup> the poisoning of Pd on supported activated carbon and  $\gamma$ -alumina during the HDC of TCE [55]. They concluded that hydrophilic support,  $\gamma$ -alumina in their case, has more affinity to Cl<sup>-</sup> ions due to acidic sites and their strengths. Similar to SOMS, polydimethylsiloxane (PDMS) support was also utilized by Comendella et al. for long-term protection of Pd nanoparticles catalyzing the HDC of chlorobenzene, TCE, and chloroform [30].

Nickel is another non-noble transition metal having activity toward HDC since Ni has also hydrogenating properties and nature. Nickel is almost 4 orders of magnitude

more abundant than Pd, Pt-like noble metals in the earth's crust [56]. Hence, this makes Ni a cost-efficient alternative to common noble metal catalysts used for HDC. Ni can also be competitive for applicational use comparing the activity with Pd for gas phase HDC at elevated temperatures as it was reviewed for HDC of chlorinated aromatics by Keane [25]. Nickel-based catalysts are generally active for HDC for the gaseous phase reactions at atmospheric pressures and elevated temperatures. Raney nickel can be an exception to this phenomenon. Raney Ni has been demonstrated to catalyze HDC of chlorophenols, and trichlorobenzene in the presence of NaOH and KOH [57], [58]. Ni/C composite catalyst was also utilized for HDC of chlorobenzene in the liquid phase however, the reaction was conducted at 70 °C and 10 bar [59]. Bimetallic Ni-Pd core-shell nanoparticles have also been applied for the HDC of 4-chlorophenols as a recoverable catalyst at ambient conditions [60]. However, the contribution of nickel nanoparticles placed inside the inner shell of Ni-Pd was a magnetic agent rather than a major catalyst since Ni has ferromagnetic properties making nanoparticles simply controllable by an external magnet for recovery of the used catalyst. Liquid phase HDC of TCE was studied over Ni-impregnated mesoporous carbon and Ni-exchanged FAU and MFI type of zeolites at ambient conditions [38], [61]. It was claimed that they have remarkable catalytic HDC activity with highly selective dechlorinated hydrocarbon products. These findings conflict with the rest of HDC literature on Ni-supported catalysts presented so far. The reported loss of TCE concentration in the solution was most likely caused by the adsorption yet not due to the catalytic HDC.

TCE vapors from big plants that typically use chemical or incinerator oxidation processes can be treated using gas phase HDC of TCE [26]. Switching from batch to continuous operation is also significant because economies of scale support continuous processes for high throughput.

HDC of chlorinated ethenes has been also studied over Ni-loaded porous materials such as zeolites, SiO<sub>2</sub>,  $\gamma$ -alumina, and recently MOFs [37], [38], [43], [62]–[64]. The first studies were carried out under high pressure (50 and 100 bar) and high temperature (300 °C and 350 °C) by Ordonez and Martino utilizing batch and flow

reactors respectively [43], [62]. In recent years, Srebowata et.al. has studied gas phase HDC of TCE and 1-2 dichloroethane (DCE) with Ni-impregnated BEA zeolites having Si/Al=17 and 1300 [38], [64]. They concluded that highly siliceous (Si/Al=1300) dealuminated BEA-supported Ni is a very efficient catalyst for HDC of DCE in terms of selectivity to ethylene and deactivation of the catalyst. However, the selectivity towards ethylene was not the same for HDC of TCE with the same catalyst yet it was still the more stable catalyst. Improvement of catalytic selectivity and deactivation resistance on the dealuminated Ni-BEA contributed to the combination of Ni incorporation and distribution on zeolites and modified acidic properties of BEA support. Ordonez et.al. also suggested chloride ions' affinity to catalyst increases with more acidic support [55].

In this study, ion-exchanged Mordenite (MOR) type zeolite was utilized as catalytic support. Mordenite has a 1-D dimensional pore channeling with a large size of ~0.67 nm 12 member-ring pore openings therefore it is widely used as a solid acid catalyst for isomerization reactions [40]. 1-D structure of MORs has the potential to render itself a straightforward support material with minimal support structure-induced effects on the HDC of TCE chemistry.

Considering the size (0.56 nm kinetic diameter) of the TCE molecule [65], it could also be very beneficial to understand the deactivation of HDC of TCE in a more controllable way with the 0.67 nm size 1-D 12-MR pore openings.

There are different approaches to obtaining hierarchically structured zeolites. Among different strategies and methodologies, dealumination is one of the most commonly used post-synthetic approaches [42], [65], [66]. Different acids such as HCl, HNO<sub>3</sub>, and oxalic acid were utilized in different studies [67]–[69]. In comparison with different acids, nitric acid provided the mordenite with the highest external surface area, mesoporous volume, and Si/Al ratios [42], [68]. Herein 6 M and 13 M nitric acid concentrations were chosen. Many studies used mild leaching concentrations such as 6 M or multiple treatments with lower concentrations[42]. However, 13 M nitric acid treatment was also performed over MORs successfully by Al-Nayili et.al considering the stable framework structure of MOR [70]. To

determine a relationship between catalytic activity and modifications upon textural and chemical properties of untreated and dealuminated MORs certain characterization techniques like N<sub>2</sub> physisorption, ICP-OES, XRD, and DRIFTS of adsorbed pyridine were executed in the scope of this study.

The degree of dealumination was found to be an important structural property that determines the catalytic activity and stability of the synthesized catalysts without major changes in the reaction mechanism.

To the best of our knowledge, Zeolite with MOR type of framework has not been tested as both catalyst and support over HDC of TCE reactions so far.

## CHAPTER 3

### EXPERIMENTAL PROCEDURES

#### 3.1 Chemicals and Materials

Trichloroethylene with a purity of  $\geq 99.5\%$  was purchased from Sigma-Aldrich. Ammonium  $\text{NH}_4$ -Mordenite with a molar ratio of  $\text{Si}/\text{Al}=10$  was purchased from Alfa-Aesar.  $\text{Ni}(\text{NO}_3)_2 \cdot 6\text{H}_2\text{O}$  salt was purchased from Supelco. Deionized (DI) water with a resistivity of  $\approx 18 \Omega \cdot \text{m}$  was used for synthesis. Pure pyridine, EMPLURA® was purchased from Sigma Aldrich. 65%  $\text{HNO}_3$  solution was purchased from Sigma-Aldrich.  $\text{H}_2$  and Ar gases (99.999% purity) were purchased from Linde.

#### 3.2 Catalyst Preparation

Mordenites are dried at  $120^\circ\text{C}$  for 1 h to remove the water adsorbed from the air. Then they were subsequently calcined under static air at  $550^\circ\text{C}$  for 4 h with a heating rate of  $2^\circ\text{C}/\text{min}$  to obtain the protonic form of  $\text{H}^+\text{MOR}$ . According to following equation 3.1.



##### 3.2.1 Dealumination of the Mordenite Support

After calcination of ammonium mordenites, dealumination was performed using 6 M or 13 M  $\text{HNO}_3$  (20 ml/g<sub>cat</sub>) at  $80^\circ\text{C}$  for 3 h under reflux. Dealuminated MORs were washed with DI water, vacuum filtrated, and left in the oven for drying at  $80^\circ\text{C}$ . Following drying, samples were washed again with 100 mL deionized water at  $80^\circ\text{C}$  to ensure that no external species like external framework alumina (EFAI) were left over the zeolite surface and in the pores. After that, samples were calcined

at 550 °C for 1.5 h to sweep up the water and nitrate species. The dealuminated samples were labeled as XM-HMOR where x indicates the concentration of HNO<sub>3</sub>. Figure 8 illustrates the dealumination steps with the equipment used in each step.

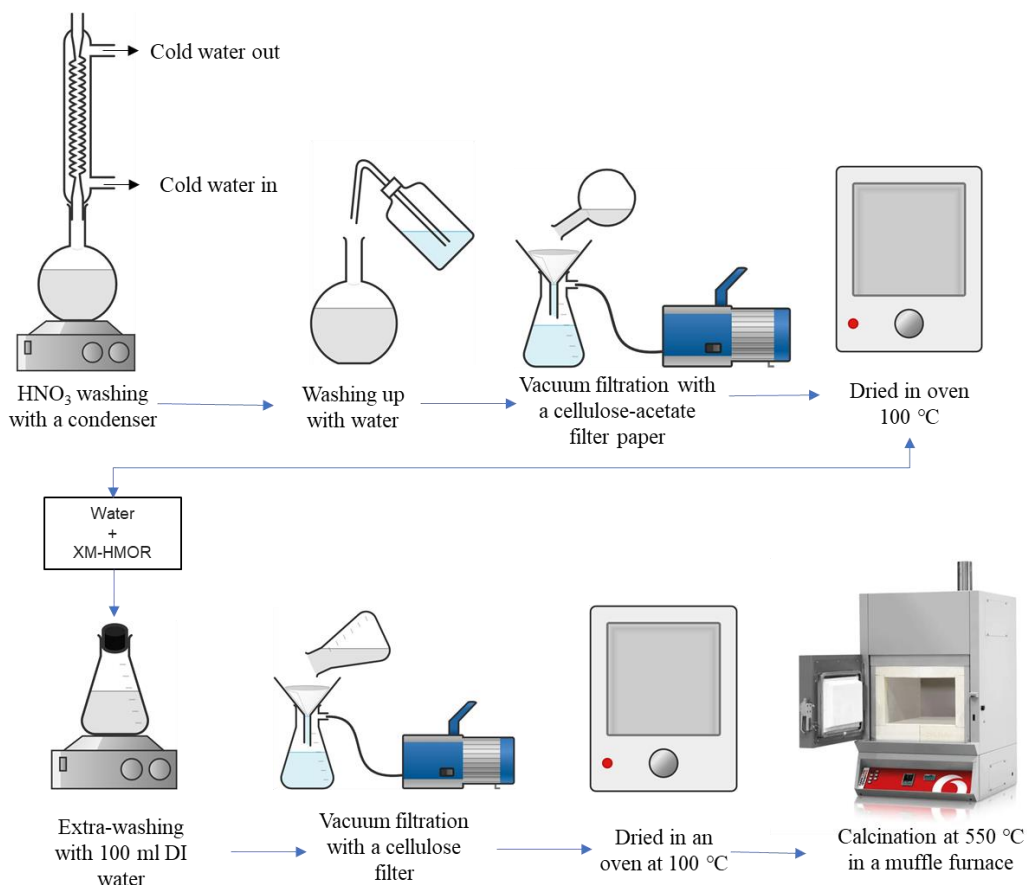


Figure 8. Experimental scheme for dealumination of HMORs.

### 3.2.2 Ni Incorporation via Ion-Exchange

Metal loading was carried out by conventional ion exchange method using an aqueous solution of 0.2 M Ni(NO<sub>3</sub>)<sub>2</sub>·6H<sub>2</sub>O precursor for 12 h at 60 °C. Metal exchanged samples were vacuum filtrated and dried at 80 °C. Following drying, the same ion exchange procedure was repeated one more time to increase metal loading. Dried samples were calcined at 500 °C for 1 h with a heating rate of 2 °C/min and reduced under pure H<sub>2</sub> at 650 °C.

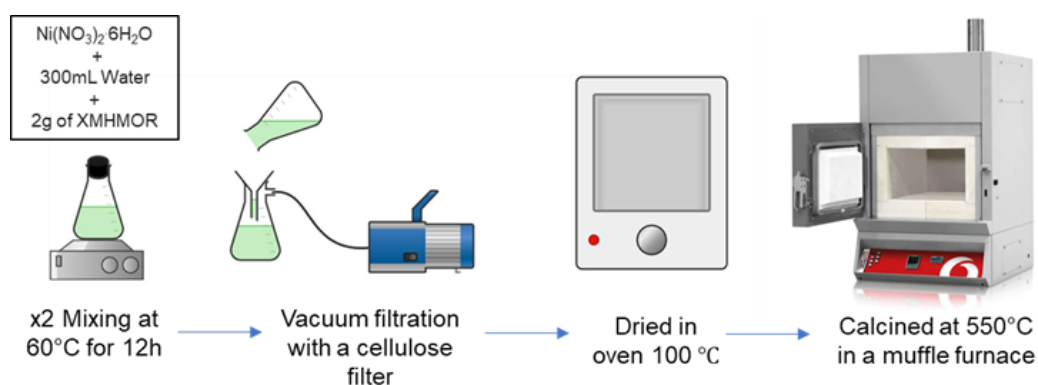


Figure 9. Schematic of nickel exchange procedure for XMHMORs

### 3.3 Characterization Experiments

#### 3.3.1 Inductively Coupled Plasma – Optical Emission Spectroscopy (ICP-OES)

The elemental analysis of bare and Ni-loaded MORs was performed using the Perkin Elmer Optima 4300DV ICP-OES instrument to obtain Si/Al ratios and Ni loading.

#### 3.3.2 N<sub>2</sub> Physisorption Experiments

Textural properties including surface area, pore size, and pore volume were obtained using Micromeritics TriStar II 3020 with the N<sub>2</sub> physisorption technique. Before analysis, samples were degassed at 300 °C for 6 h under a vacuum to remove the moisture and undesired species from the sample. Physisorption experiments were performed at 77 K. Surface area of samples and pore size distribution were analyzed by the Branauer Emmer Teller (BET) and Barrett-Joiner-Halenda (BJH) adsorption methodologies. T-plot micropore volume and BJH desorption cumulative area of the pores were obtained to understand changes in structure and mesoporous volume as well as BET and external surface areas.

### **3.3.3 Temperature Programmed Reduction under H<sub>2</sub> (H<sub>2</sub>-TPR)**

H<sub>2</sub>-TPR experiments were conducted using a quartz reactor (I.D.= 4.5 mm) loaded with catalyst powders (mesh size = 40-70, 170 mg) that were supported from both ends using quartz wool to form a reactor bed with a height of 20 mm. The reactor is then placed in a tubular furnace and temperature measurements were performed using a thermocouple outside the bed. Before reduction, samples were oxidized at 550 °C for 1 h with 30 sccm of 7% O<sub>2</sub>/Argon to remove adsorbed water and other carbonaceous species. The reactor was then cooled down to room temperature and reduction was started with a flow rate of 30 sccm pure H<sub>2</sub> and a ramp rate of 10 °C/min up to 1000 °C. The exhaust gas composition was monitored with an on-line residual gas analyzer (Hiden Analytical HPR20 Mass Spectrometer). Mass to charge (m/z) ratios of H<sub>2</sub> and H<sub>2</sub>O as well as other relevant signals were monitored simultaneously with the increasing temperature of the reactor.

### **3.3.4 Post Reaction Temperature Programmed Hydrogenation (TPH)**

TPH experiments were conducted using a quartz reactor (I.D.= 4.5 mm) loaded with catalyst powders (mesh size = 40-70, 90 mg) that were supported from both ends using quartz wool to form a reactor bed with a length of 14 mm. Catalytic reaction was conducted as described in Chapter 3.4. After approximately 6 h of reaction and cooling to room temperature from 300 °C, exit of the reactor stream was connected to Hiden Analytical HPR20 Mass Spectrometer while Argon constantly flowing out from the reactor exit to prevent major air contact with the used catalyst. Under Argon flow, reactor was stabilized for 30 min at room temperature. Then flow was changed to pure H<sub>2</sub> with a flow rate of 30 sccm. After stabilization reactor heating was started from room temperature to 950 °C with a 10 °C/min ramp. Mass to charge (m/z) ratios of HCl (36, 38 signals), CH<sub>4</sub> (15,16 signals), H<sub>2</sub>, H<sub>2</sub>O (17,18) and other required molecules were monitored simultaneously with the temperature of the reactor.

### **3.3.5 CO Pulse Chemisorption**

CO chemisorption of differently prepared Ni-MORs was conducted to quantify metal dispersion and accessibility of active Ni sites. The reactor and heating system is the same as the H<sub>2</sub>-TPR system with an addition of a six-port valve to be able to introduce CO gas pulses to the flow system. Ni-MORs were reduced before CO chemisorption. All samples were reduced with pure hydrogen in a gas phase system at 650 °C for 1h with a heating rate of 5 °C/min under Ar flow. After reducing catalysts, reactor was cooled down to 40°C under Ar flow. Chemisorption experiments were conducted at 40 °C. CO pulses were recorded and maintained until saturation was observed through MS software. Ni to CO uptake ratio was assumed 1:1 and calculations were done based on this assumption as suggested in by different studies [54], [71], [72]. Dispersion of the nickel was calculated as “moles of Nickel reacted with CO/moles of Ni in the sample”.

### **3.3.6 X-Ray Diffraction Analysis (XRD)**

The crystal structure of the untreated and post-dealuminated MOR supports as well as Ni-XM-MORs were analyzed by Rigaku Ultima-IV X-Ray powder Diffraction instrument. Scanning data were recorded with the interval of  $2\theta=2-50^\circ$  and a step size of  $1^\circ/\text{min}$ . International Zeolite Association (IZA) database was used for data analysis [73].

### **3.3.7 X-Ray Photoelectron Spectroscopy (XPS)**

K-alpha Thermo Scientific XPS was used to analyze specific elemental bonding states of HDC used catalyst. Monochromatic Al K $\alpha$  X-Ray source was used. Energy of photons coming from X-ray source was 1486.6 eV, and spot size was arranged as 400  $\mu\text{m}$ . Peaks were deconvoluted by using CasaXPS software. Ni, Al, Cl, Si, O and C elements were analyzed within their specific binding energy ranges.

### **3.3.8 In-Situ Diffuse Reflectance Infrared Fourier Transform Spectroscopy (DRIFTS) of Adsorbed Pyridine**

Bronsted and Lewis acid sites (BAS and LAS) were characterized in-situ by DRIFTS of adsorbed pyridine in a praying mantis™ high-temperature reaction chamber (Harrick Sci). Before pyridine adsorption, samples were treated at 500 °C under 30 sccm Ar flow for 3 h, and then cooled to 50 °C while collecting background spectrum at 450 °C, 350 °C, 250 °C, 150 °C, and 50 °C. Then, pyridine vapor was adsorbed on the sample at 50 °C for 30 min. Following the pyridine adsorption, the cell was purged with Ar for 20 min and sample spectrum was collected. The temperature was then increased at 100 °C increments and sample spectrum were collected at each temperature where background was collected. DRIFTS spectra were recorded with a FTIR equipped with a liquid N<sub>2</sub>-cooled MCT detector. Spectra were obtained in absorbance mode between 900 cm<sup>-1</sup> and 4000 cm<sup>-1</sup> with 512 scans and a resolution of 2 cm<sup>-1</sup>. The spectrum subtraction was performed using the FTIR instrument's software.

### **3.3.9 Thermogravimetric Analysis (TGA) of Spent Catalysts**

Thermogravimetric analysis was performed using Shimadzu DTG-60H Thermogravimetric Analyzer to examine the formation of carbonaceous deposits under reaction conditions. TGA experiments were carried out under dry air by heating from room temperature to 900 °C with a ramp rate of 10 °C/min. The rate of mass change with temperature was monitored and recorded by TGA software.

### **3.3.10 High-Resolution Transmission Electron Microscopy (HR-TEM) sample preparation**

HRTEM images of each reduced sample were taken by FEI TALOS F200S TEM 200 kV and Jeol JEM 2100F HRTEM, 200kV to identify the particle sizes of nickel

nanoparticles on Ni-xM-HMORs. Images of every sample were taken several times to assure uniformity of particles throughout the zeolite clusters and to have a correct average particle size distribution.

### **3.4 Catalytic Aqueous Phase HDC Activity Tests**

Aqueous phase reactions were conducted at room temperature and atmospheric pressure. Firstly, reactor with a total volume of 800 mL was filled with 500 mL of deionized water. Second step was to feed Argon gas for 60 min to carry the atmospheric gases out from the reactor. Then H<sub>2</sub> was introduced for another 60 minutes to saturate the water and headspace of the reactor with H<sub>2</sub> gas. Thirdly TCE was injected to reactor as 1 mL ethanol and TCE mixture. After waiting 30 minutes for equilibration under constant mixing, 10 mg of previously reduced catalyst was injected as water catalyst suspension and reaction was initiated. During the reaction Cl<sup>-</sup> concentration was recorded with Hanna HI-4107 Ion Selective Electrode (ISE). Figure 10 illustrates the scheme of the aqueous phase batch reactor system.

To analyze side products formed during the reaction, samples from the reactor were also taken in certain time intervals to be analyzed by High-Pressure Liquid Chromatography (HPLC) equipped with a UV-vis detector (Shimadzu, SPD20A). HPLC was operated with single mobile phase. Mobile phase composed 25% water and 75% acetonitrile by volume. Samples were separated in a column of Merck Purospher® with 5 µm packing. Results were plotted based on wavelength of 199 nm data collected by UV-vis detector. In addition to the 199 nm, 204 nm was also tracked and both wavelengths revealed fairly consistent results.

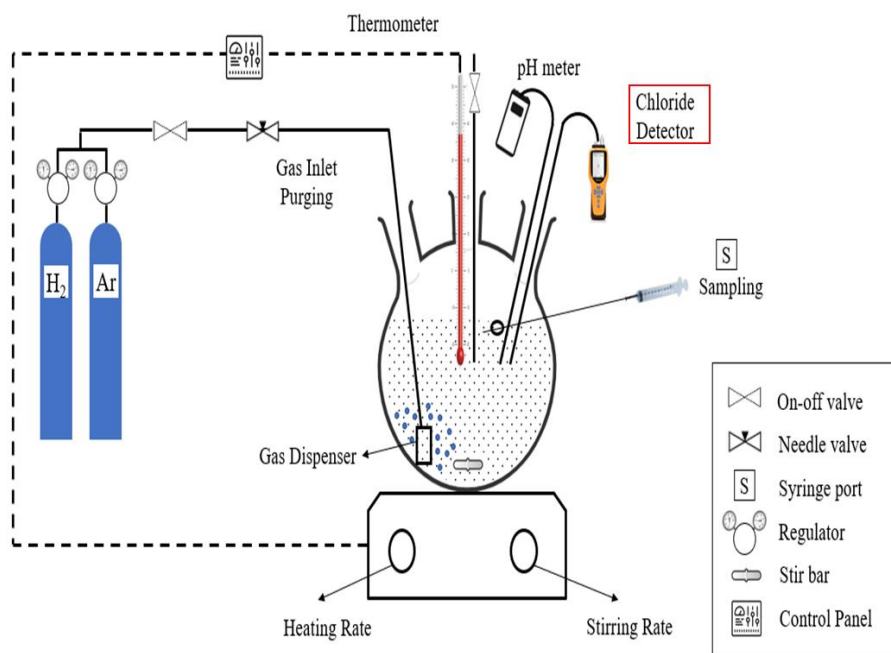


Figure 10. Experimental set-up for aqueous phase HDC tests.

### 3.5 Catalytic Gas Phase HDC Activity Tests

Catalytic gas phase HDC of TCE experiments were conducted over ion-exchanged Ni-xM-HMORs using a fixed-bed quartz reactor with an I.D. of 0.45 cm. Catalyst samples (typically 30 mg) were loaded to the reactor and supported in the middle of it by quartz wool on both sides. The reactor is located in a tubular furnace and connected to the gas manifold. The reactor temperature was controlled by using Eurotherm 3208 temperature controller which is connected a thermocouple placed outside the reactor, but right next to the catalyst bed.

TCE is introduced to the gas manifold through a bubbler at room temperature using Ar as the sweep gas. The feedstock composition was 1.2 % TCE, 82%  $H_2$  by volume and balance Ar.  $H_2$  to TCE molar ratio is more than 60, providing excess  $H_2$  conditions and setting TCE as the limiting reactant. The gas hourly space velocity through the reactor bed is approximately  $25,000\text{ h}^{-1}$  with a total flow rate of the feed gas  $30\text{ cm}^3/\text{min}$  (sccm).

Catalysts were reduced before the reaction with a pure H<sub>2</sub> flow for 1 h at 650 °C. Catalytic activity experiments were conducted at 300 °C. The unconverted reactant and products were analyzed by an online gas-chromatography (Perkin Elmer Clarus 500) equipped with a six-port valve for sampling, an 80/100 mesh-sized Poropak Q packed column for separation and a flame ionization detector for quantification. GC oven temperature profile consisted of three steps: (i) dwell at 70 °C for 5 min, (ii) ramp to 150 °C with a rate of 10 °C/min, and (iii) dwell at 150 °C for 25 min. TCE conversion and selectivity values were calculated according to Eq. 1. and 2 as given in Appendix A. Carbon balance was performed to ensure the mass balance of the system. A carbon balance of 96% or higher was obtained. Chloride balance was not performed. Schematic of gas phase HDC activity system is shown in Figure 11.

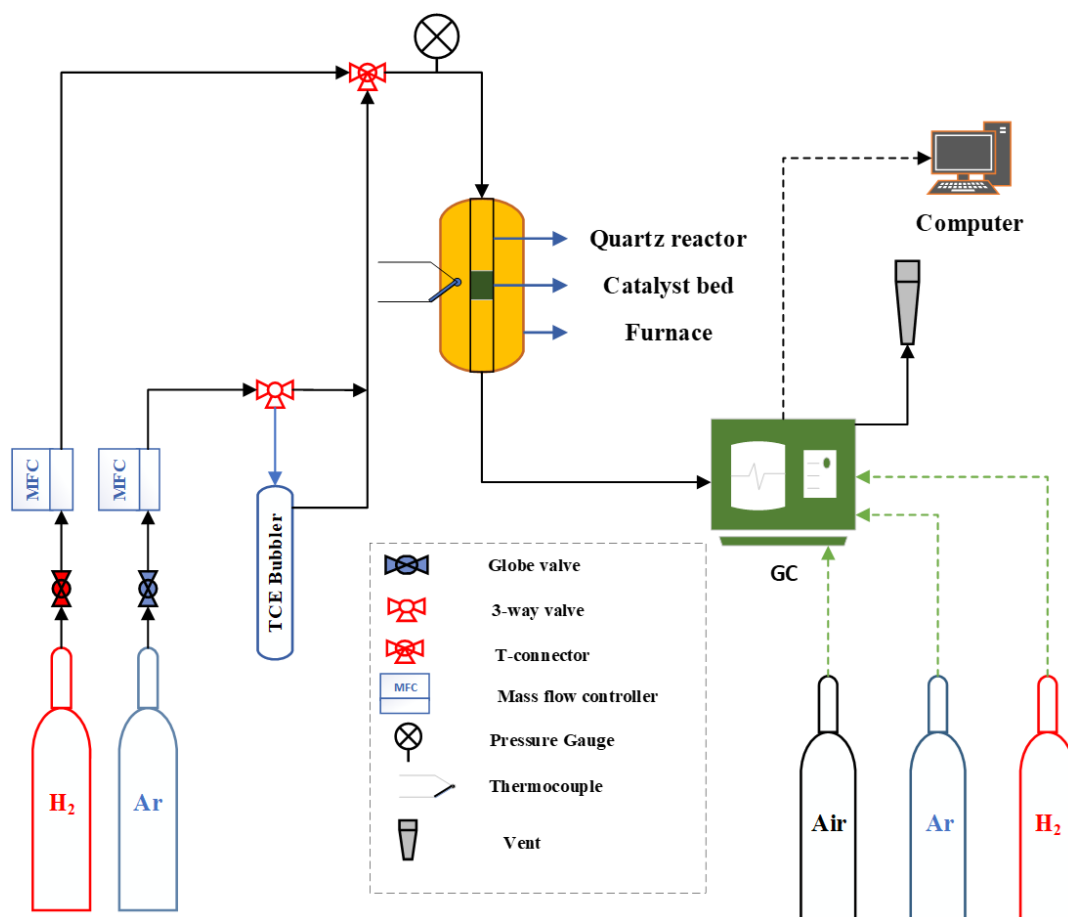


Figure 11. Flow Diagram of gas phase HDC activity system

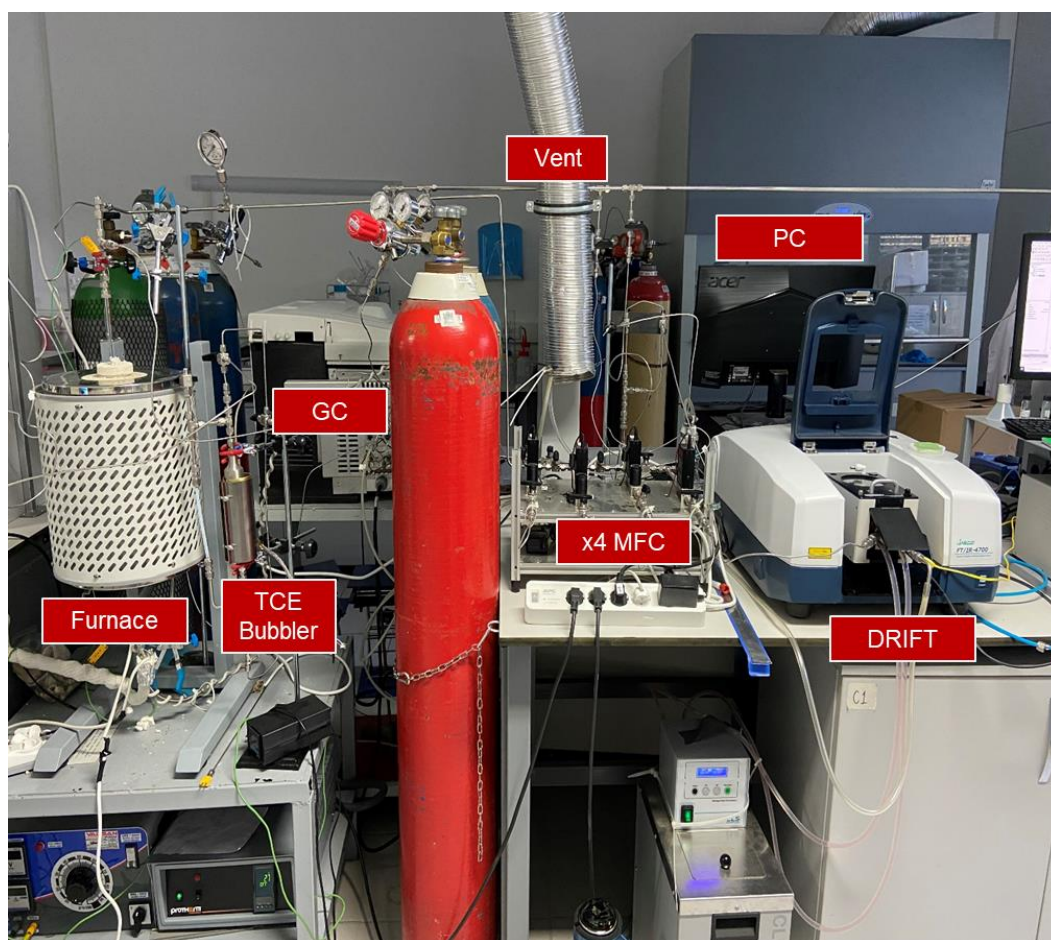


Figure 12. Picture of HDC activity system and its major components in series with in-situ DRIFTS system

## CHAPTER 4

### RESULTS AND DISCUSSIONS

#### 4.1 Dealumination of Mordenite Support

##### 4.1.1 N<sub>2</sub> physisorption Results of XM-HMORs and Ni-XM-HMORs

N<sub>2</sub> physisorption experiments were performed to examine raw and post-synthesized mordenite samples in terms of their surface area, pore volumes, and pore sizes. Tabulated values are provided in Table 1. The highest BET surface area was obtained over 6 M acid leaching as 472 cm<sup>3</sup>/g whereas the lowest was obtained over 13 M acid leaching as 442.6 cm<sup>3</sup>/g. The external surface of the MOR support is raised with the concentration of acid treatment. It can be said that micropore volume was preserved over acidic treatment for both 6MHMOR and 13MHMOR samples. The mesoporous volume of MOR has also slightly enhanced over acid treatment where the highest meso volume was obtained for 6MHMOR as 0.11 cm<sup>3</sup>/g. Table 1 also represents Si/Al ratios of dealuminated and bare MORs which were analyzed by ICP-OES and the Si/Al increases from 9.6 to 58.3 and 101.4 upon dealumination with 6 M and 13 M nitric acid respectively.

Adsorption-desorption isotherms of the HMOR, 6MHMOR, and 13MHMOR examples are provided in Figure 13a. The isotherms in Figure 13a exhibit type IV isotherms where monolayer-multilayer adsorption and capillary condensation take place [74]. The inset in Figure 13a represents the start of hysteresis in which no considerable change in mesoporosity is observable as shown from the tabulated values. The microporous structure is still dominant for dealuminated samples even after concentrated nitric acid washings as seen from both adsorption-desorption isotherms and BJH pore size distribution plots. To create considerably large mesoporous structures desilication is preferably applied in most of the studies [75].

BJH adsorption isotherms and the pore size distribution of XMHMORs were also obtained as represented in Figure 13b. For randomly distributed pores and an interconnected pore system, the desorption branch is more prone to be affected by pore network effects and tensile strength effect phenomena. Hence, using the adsorption branch for pore size distribution for zeolites is suggested in the literature [74]. There is a sharp increase in the microporous regime (<1 nm) for all three samples. A slight increase around 7 nm was observed for dealuminated samples and this small jump also coincides with BJH adsorption isotherms. 6MHMOR has shown higher mesoporosity than 13MHMOR contrary to expectations. However, the 13MHMOR sample underwent major modifications where considerable crystal size reduction was observed, as discussed in section 3.1.2. N<sub>2</sub> physisorption results revealed a modest enhancement in mesoporosity and external surface area upon dealumination by preserving primary microporous structure of MOR.

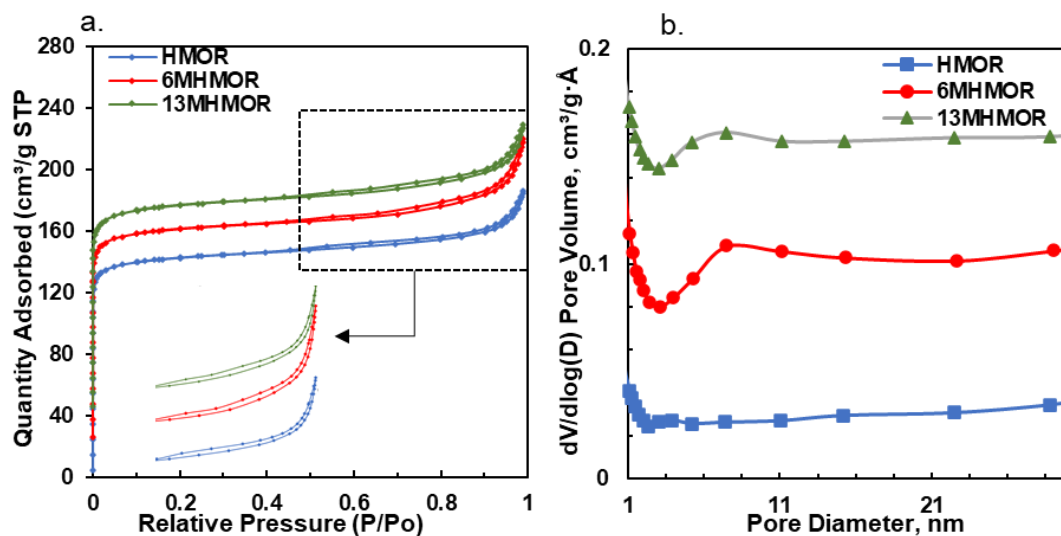


Figure 13. (a) Nitrogen adsorption-desorption isotherms, Inset: hysteresis, and (b) BJH adsorption pore-size distribution of bare and dealuminated MORs

Table 1. Textural properties and elemental analysis of bare and dealuminated MORs.

Sample	BET Surface Area (m <sup>2</sup> /g)	t-Plot External Surface Area (m <sup>2</sup> /g)	t-Plot micropore volume (cm <sup>3</sup> /g)	Mesoporous Volume (cm <sup>3</sup> /g)	Single point adsorption total pore volume (cm <sup>3</sup> /g)	BJH Desorption average pore diameter (4V/A) (nm)	Si/Al
<b>HMOR</b>	462	56	0.20	0.08	0.28	6.4	10
<b>6MHMOR</b>	472	64	0.20	0.10	0.30	7.5	58
<b>13MHMOR</b>	443	70	0.18	0.10	0.28	6.6	101

#### 4.1.2 X-Ray Diffraction Results of Dealuminated MORs

The zeolite's structure changed after dealumination by nitric acid extraction because the framework Al atoms were dissociated from the zeolite's framework. Depending on the acid concentration and treatment circumstances, severe transformations can be observed in the zeolite structure. Since dealumination was carried out with rather concentrated acid solutions, some textural analyses (BET, XRD) must be executed to confirm any phase and structural changes. Even though previously completed BET analysis provides some hints regarding the morphological change, it was still necessary to conduct an X-Ray Diffraction (XRD) crystallography analysis to verify the zeolite structure. Untreated and dealuminated zeolites produced the same XRD patterns obtained as in Figure 14. Diffraction angles of characteristic peaks for all 3 samples are 6.54°, 8.76°, 9.78°, 13.56°, 15.30°, 19.74°, 22.40°, 25.8°, 26.4°, 27.74°, and 31.06° coinciding with the International Zeolite Association Database (IZA-online) and other studies in the literature [73], [76], [77]. The phase of the MORs corresponds to the orthorhombic phase as verified by JCPDS data, card no.: 430171 by Narayanan et.al. [76]. Peak intensities at low diffraction angles which are lower than 10°, increased over dealuminated samples compared to bare HMOR. This can be attributed to the enhanced hydrophobicity, loss of acid sites, and non-framework species formed after the dealumination step [40]. Since the aluminum atoms

especially positioned in tetrahedral coordination within the zeolite cages, intensity of certain peaks such as 6.54 and 9.7 showed higher intensity. Increase in this can be attributed to new chemical structures formed with Si and OH groups within the zeolite framework. Characteristic peaks and general crystal structure are confirmed to be preserved over dealumination with 6 M and 13 M nitric acid treatments as seen in Figure 14. However peak intensities of 13MHMOR sample were clearly decreased in between 10° and 40°. Severe Al extraction from the structure causes the intensity decreases for 13MHMOR sample.

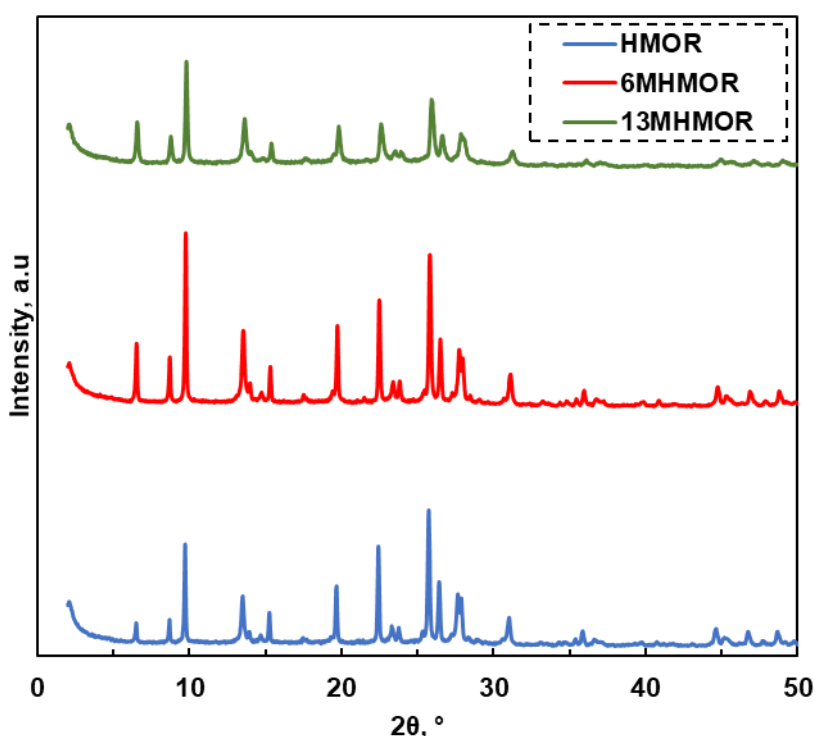


Figure 14. X-Ray diffraction patterns of untreated and dealuminated MORs.

Crystal size of the zeolite particles were calculated according to Scherrer equation as given in equation 4.1.

$$L = \frac{0.89\lambda}{\beta \cos\theta} \quad \text{Eqn. 4.1}$$

L represents the average crystal size,  $\lambda$  the wavelength of the X-ray which is accepted as 0.154 nm and  $\beta$  is the full width at half maximum (FWHM) with a unit of radian. Average crystal size calculated according to diffraction peak located at 26.4 [76]. Crystal sizes of the bare and dealuminated samples were found as in Table 2. Crystal size of 6MHMOR sample was not changed considerably upon dealumination. However, almost 40% decrease in crystal size was observed for 13MHMOR.

Table 2. Crystal sizes of bare and dealuminated MORs,

	Crystal size (nm)
<b>HMOR</b>	47.3
<b>6MHMOR</b>	46.2
<b>13MHMOR</b>	29.9

#### 4.1.3 DRIFTS of Adsorbed Pyridine Results over Dealuminated MORs

Surface acidity is one of the most important features of zeolites, especially in catalysis applications. Different base precursors such as ammonia, pyridine, acetonitrile, etc. have been utilized to enlighten the acidic properties of solid acids [78]. Pyridine is the most commonly used and reliable precursor in terms of determining acid site densities [79]. It is also more convenient to use a precursor, pyridine kinetic diameter=0.53 [80], with similar size of reactant molecule, the kinetic diameter of TCE=0.56 nm [65], for a better assessment of acid sites in catalytic activity [40]. DRIFTS was used to track the temperature-programmed desorption (TPD) of pyridine in order to examine the acidic characteristics of dealuminated and raw mordenite. With the increase in Si/Al ratios, acidic properties of zeolites were also modified by creating differently coordinated -OH bonds through the framework such as silanol groups or -OH coordinated at extra framework aluminum and silicon [40], [66], [81], [82]. Figure 15 represents the DRIFTS absorbance spectrum of adsorbed pyridine for all three samples. Unlike desilication, dealumination reduces the number of acid sites confined in zeolites since the mesopores are created by extracting framework Al, which initially poses acid sites

[69]. This trend was also verified in our study as seen in Figure 15 higher the degree of dealumination lower the number of acid sites.

As the concentration of acid treatment increases the intensity of the peaks at 1590  $\text{cm}^{-1}$  and 1580  $\text{cm}^{-1}$  also increase. These two peaks are attributed to H-bonded pyridine acting as Bronsted acid site (BAS) and physisorbed pyridine respectively [82], [83]. The increase in protonated BAS at 1590  $\text{cm}^{-1}$  is most likely associated with the increase in Si-OH (silanol) groups formed throughout the defects on external surfaces. A small peak at 1580  $\text{cm}^{-1}$  loses intensity at 150 °C and above 150 °C no distinguishable peak is observed confirming that corresponds to physisorption for all three samples. Peaks at 1445  $\text{cm}^{-1}$  and 1620  $\text{cm}^{-1}$  are considered coordinatively bonded pyridine to Lewis acid sites (LAS) [82]. The intensity of LAS at 1450  $\text{cm}^{-1}$  shows a very slight decrease by acid treatment and does not change considerably in between the 6MHMOR and 13MHMOR samples. The shoulder peak at 1620  $\text{cm}^{-1}$  also shows a decreasing trend with respect to increasing acid treatment concentration. Peaks at 1541  $\text{cm}^{-1}$  and 1486  $\text{cm}^{-1}$  are considered chemisorbed pyridine on a strong combination of LAS and BAS and they are generally with structural bridging silanol (Si-OH-Al) groups where OH groups are strongly coordinated and bonded to Si and Al atoms [83], [84]. For the 6 M dealuminated sample, 1541  $\text{cm}^{-1}$  and 1486  $\text{cm}^{-1}$  peaks still exist however in a negative direction meaning that they became considerably weaker acid sites so that they could be desorbed by pyridine during Ar flush as in Figure 15b. Lastly, these initially strong sites were not observed as the spectrum in Figure 15c presents nothing but noise over 13 M  $\text{HNO}_3$  dealumination. Loss of strong acid sites upon dealumination also demonstrated homogeneous acid leaching of Al atoms coordinated at tetrahedral sites of the framework.

TPD represents the acidic property of dealuminated samples that are not efficient beyond 350 °C since no pyridine adsorption peaks were observed on 6MHMOR and 13MHMOR. On the other hand, HMOR peaks at 1541  $\text{cm}^{-1}$  and 1486  $\text{cm}^{-1}$  are well preserved up to 450 °C demonstrating the strong acid-base interaction with pyridine molecules. Peaks between 1577  $\text{cm}^{-1}$  and 1640  $\text{cm}^{-1}$  are not distinguishable above

250 °C as lower temperatures for HMOR but they are still present on the structure due to the positive absorbance on the spectrum. LAS at 1455 cm<sup>-1</sup> also gradually decreases with increasing temperature for HMOR as in Figure 15a. These results showed that the acidity of the mordenite samples was tuned both quantitatively and qualitatively by the dealumination procedure.

Table 3. Peak assignments for bare and dealuminated MORs over pyridine DRIFTS.

<b>Mode of ring vibrations</b>	<b>HMOR</b>	<b>6MHMOR</b>	<b>13MHMOR</b>	<b>Peak Assignment</b>
<b>19b</b>	-	-	-	H-bonded pyridine
<b>19b</b>	1445	1445	1445	Pyridine on weak BAS
<b>19b</b>	-	-	-	Pyridine on LAS
<b>19a</b>	1486	-	-	Chemisorbed pyridine on LAS+BAS
<b>19b</b>	1541	-	-	Protonated pyridine on BAS
<b>8b</b>	-	-	-	Chemisorbed pyridine
<b>8a+8b</b>	1577	1580	1580	Physisorbed pyridine
<b>8a</b>	1590	1590	1590	H-bonded pyridine
<b>8a</b>	1608	-	-	Pyridine bonded to octahedral LAS
<b>8a</b>	1626	1626	1626	Pyridine on LAS
<b>8a</b>	1638	-	-	Protonated pyridine on strong BAS

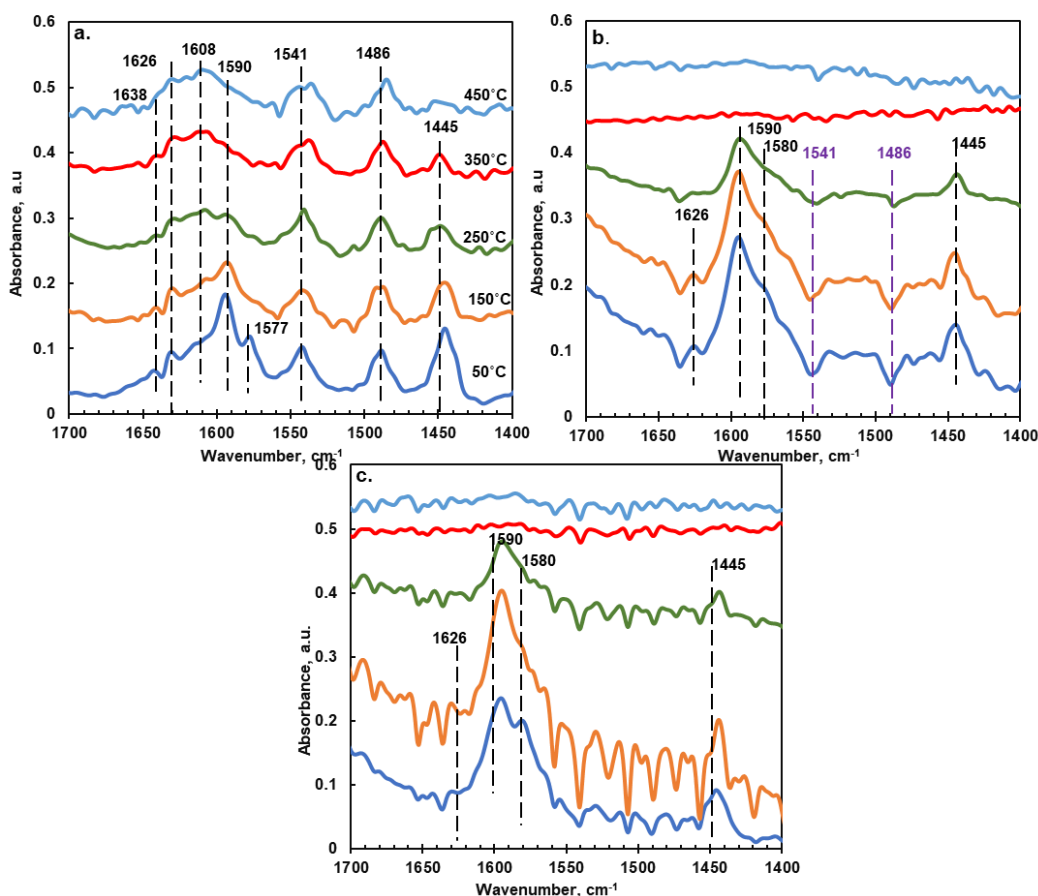


Figure 15. DRIFTS spectra of adsorbed pyridine over (a) HMOR, (b) 6MHMOR, and (c) 13MHMOR from 50 °C to 450 °C.

## 4.2 Ni loading to XM-HMORs via Ion Exchange

### 4.2.1 ICP-OES Results

Ni was loaded to bare and dealuminated MORs via ion exchange, one of the most common post-encapsulation methods. Ni-exchanged samples were analyzed for elemental compositions by ICP-OES. Table 4 represents the elemental ratios and Ni weight percentages for each Ni-XMHMOR sample. The Si/Al ratio of samples increased as the concentration of HNO<sub>3</sub> treatment increased. The relation between the Si/Al and acid concentration is suggested to be linear. The maximum nickel amount was loaded to 6MHMOR, second to 13MHMOR, and lastly to HMOR

samples. The capacity of cation exchange for zeolites generally increases with the Al extent within the zeolite structure since Al contributes to the net negative charge of the structure as the Eisenman theory suggests [75], [85]. However, cation exchange over zeolites is also a diffusion-controlled process in which steric restrictions possessed by the zeolite framework itself bring vital importance to the degree of exchange among other diffusional constraints as herein our case. When the nickel nitrate salt dissolved in water Ni ions form complex octahedral  $[\text{Ni}(\text{H}_2\text{O})_6]^{2+}$  structures. Depending on the solution environment and material interactions the kinetic diameter of this kind of complex structure can vary in between the 0.5-0.7 nm. Considering the largest pore opening of MOR which is 0.67 nm, this could cause diffusional constraints especially for bare MOR support. When 13MHMOR is compared with HMOR, the contribution to Ni uptake cannot be attributed to the crystallinity yet the increase in the external surface area provided larger defects and vacant sites upon dealumination. This is also shown by TEM results in section 3.4 where relatively larger Ni nanoparticle formation is observed over the external surface of dealuminated MORs than bare MOR. These external framework species are easy to incorporate compared to vacant sites in micropores for the metal cations to be exchanged.

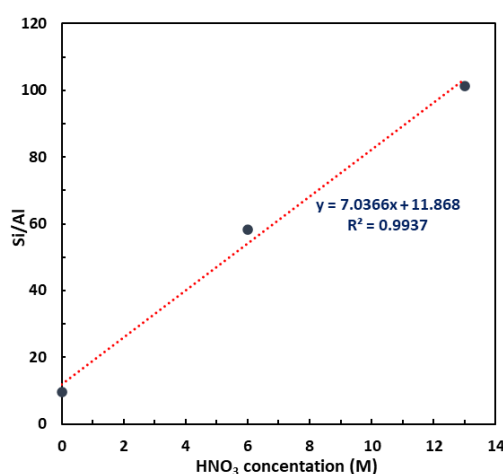


Figure 16. Dealumination acid concentration vs. obtained Si/Al ratio plot.

Figure 16 represents the linear increase in Si/Al consequent to dealumination also proposed that the external framework aluminum is completely extorted as the degree of dealumination increases. This was also demonstrated by Giudici et.al. in which HNO<sub>3</sub> nitric acid-treated MORs presented almost no EFAl whereas EFAl species were observed with oxalic acid-treated MORs [67].

Table 4. Elemental analysis of Ni exchanged HMORs dealuminated to a different extent.

Sample	Si/Al (Atomic Ratio)	Ni/Al (Atomic Ratio)	Ni (weight %)
Ni-HMOR	9.6	0.05	0.45
Ni-6MHMOR	58.3	0.37	0.60
Ni-13MHMOR	101.4	0.55	0.52

#### 4.2.2 N<sub>2</sub> Physisorption Experiments for Ni exchanged MORs

Ni-exchanged samples were also analyzed by N<sub>2</sub> physisorption experiments. Figure 17 demonstrates the adsorption-desorption isotherms and pore size distributions of Ni-exchanged samples. There were no considerable changes in isotherm types after ion exchange. Tabulated values are given in Table 5. BET and external surface areas were not considerably changed upon Ni-exchange demonstrating the Ni incorporation into a zeolite structure. Consequently, there were no major changes regarding the porous structure of the MORs after the Ni-exchange procedure.

Table 5. Textural properties of Ni exchanged XMHMORs

Sample	BET Surface Area (m <sup>2</sup> /g)	t-Plot External Surface Area (m <sup>2</sup> /g)	t-Plot micropore volume (cm <sup>3</sup> /g)	Mesoporous Volume (cm <sup>3</sup> /g)	Single point adsorption total pore volume (cm <sup>3</sup> /g)	BJH Desorption average pore diameter (4V/A) (nm)
Ni-HMOR	465.4	60.9	0.20	0.10	0.30	7.3
Ni-6MHMOR	505.0	66.7	0.22	0.11	0.33	7.8
Ni-13MHMOR	457.0	71.4	0.19	0.12	0.31	7.3

XRD patterns for reduced Ni exchanged MORs represented on Figure 35 in Appendix D. No change with respect to overall crystal structure was observed. Due to exchanged atoms in framework, peak intensities represent differentiation for all 3 catalysts.

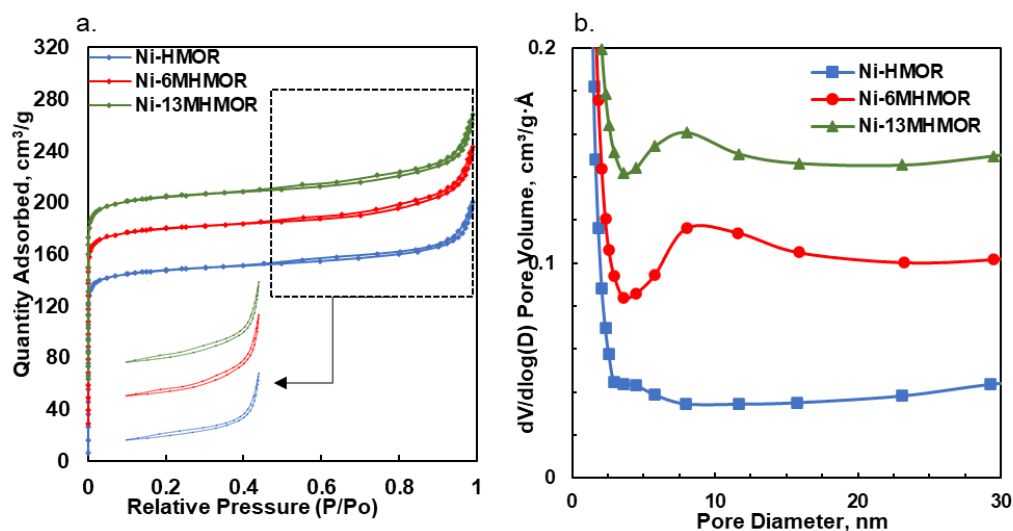


Figure 17. (a) Nitrogen adsorption-desorption isotherms, Inset: hysteresis, and (b) BJH adsorption pore-size distribution of bare and dealuminated Ni exchanged MORs.

### 4.2.3 H<sub>2</sub>-Temperature Programmed Reduction Results

To understand the reduction behavior and metal species incorporated upon the synthesized catalysts H<sub>2</sub>-TPR experiments were performed. Figure 18 represents the tracking of the formed H<sub>2</sub>O signal with respect to increased temperature during the hydrogenation of each sample with pure H<sub>2</sub>. TPR profiles of low-temperature (150–300 °C) region show different reduction temperatures for all 3 samples. These peaks generally correspond to Ni species that are in weak interaction with the supports as it was suggested by different studies working on Ni-incorporated zeolite samples [86]–[88]. However, as the dealumination of the support increased this temperature showed a decreasing trend from 290 °C to 150 °C. The low reduction temperature

profile is also likely to be caused by the mono-( $\mu$ -oxo) Ni species formed upon calcination by the O<sub>2</sub>-Ar mixture reported earlier [89]. This kind of metal zeolite species is known to have a lower reduction temperature than metallic species on zeolite [90]. The reduction temperature of nickel species that are weakly interacted with zeolite support decreases as the degree of dealumination increases. Early peak for Ni-HMOR is around 300 °C and decreases to 220 °C and 150 °C for Ni-6MHMOR and Ni-13MHMOR respectively. As the severity of dealumination increases it is more likely to have less stable and weakly interacted Ni species at the external surfaces of zeolites. Nickel species loaded as compensation cations over zeolites generally reduced at elevated temperatures above 600 °C. As shown in Figure 18, slightly broadening peak at 850 °C was observed for Ni-HMOR sample. This might correspond to the more stabilized and exchanged Nickel cations or covalently bonded nickel oxide centers located in framework tetrahedra. However, 850°C peak lowers to 650 °C for nickel supported on dealuminated samples indicating formation of possible isolated metal clusters incorporated inside the zeolite pores or strong nickel clusters positioned over the pore openings and external surface of the zeolite. There are three generally suggested incorporations of metals for zeolites which are (i) isolated large metal oxides within zeolite cages, (ii) ion-exchanged or mono-oligo nuclear complexes stabilized inside the cage, and (iii) single heteroatoms substituted into zeolite framework [91], [92]. However, the homogeneous specific distribution of these sites requires advanced synthesis procedures where certain encapsulation of metal inside the micropores still studied by different authors [93], [94]. However, these kinds of advanced techniques still require further improvements and research considering the various applications of catalysis. Thus, post-encapsulation via conventional ion exchange can possess differently incorporated metal species on both internal and external surfaces of zeolite.

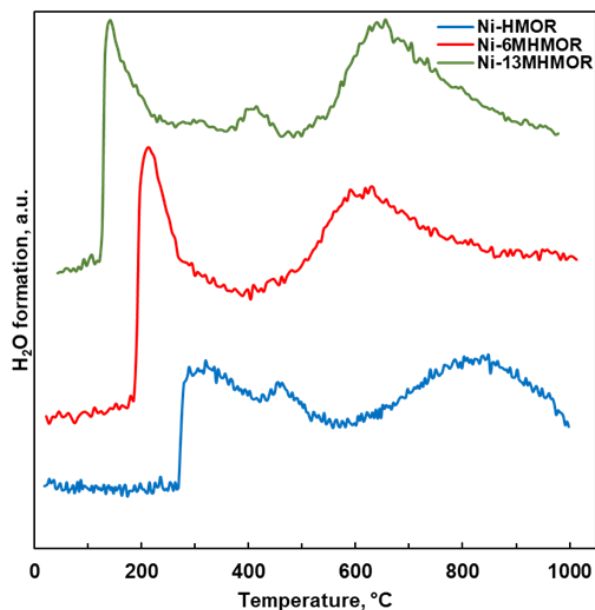


Figure 18. H<sub>2</sub>-TPR profiles of the bare and dealuminated Ni-loaded HMORs

#### 4.2.4 Nickel Particle Size Analysis by HR-TEM

The Ni particle sizes and their distribution over bare and dealuminated samples were analyzed by the HR-TEM technique. The particle size distributions of reduced Ni-HMOR, Ni-6MHMOR and Ni-13MHMOR samples were obtained as shown in Figures 19a, b, and c respectively. The smallest particles were observed with bare HMOR samples with average particle sizes of  $8\pm 1.9$  nm. For the Ni-6MHMOR sample particle sizes were obtained as  $8.6\pm 2.5$  nm. Finally, the largest average particle size distribution was acquired as  $10.1\pm 4.3$  for Ni-13MHMOR.

As mentioned in section 2.2, dealuminated and Ni-exchanged samples were reduced at 650 °C with pure H<sub>2</sub> for 1.5 h. Due to high reduction temperatures, it was expected to see Ni particles that are sintered or clustered upon thermal reduction. As a rule of thumb, metal particles gain mobility at a temperature where  $T=0.33\times T_{\text{melt}}$ , also known as Tamman temperature [78]. HR-TEM results have shown that all samples formed Ni nanoparticles which are above 3 nm after reduction. The findings imply that the extent of dealumination did not significantly influence the metal

agglomeration over the zeolite, as the average particle sizes fell within a comparable range for each sample, taking into account the inherent margins of error. This trend can be attributed to stable Ni incorporation throughout the zeolite structure. Considering the Si/Al ratio of HMOR support has the highest Al atoms in its' structure providing more cationic Ni incorporation into the zeolite framework due to the negative charge of Al atoms contributing resistance against agglomeration of Ni particles [40], [75]. A negligible increase in particle sizes of the Ni-6MHMOR sample can be associated with an increase in external surface area and the number of Nickels incorporated upon the external surface of the zeolite resulted in larger observable Ni particles. The relatively large particle size distribution of Ni-13MHMOR can be caused by its' crystal sizes and higher external surface defect. Particle size distributions in TEM pictures are in accordance with the H<sub>2</sub>-TPR results in Figure 18.

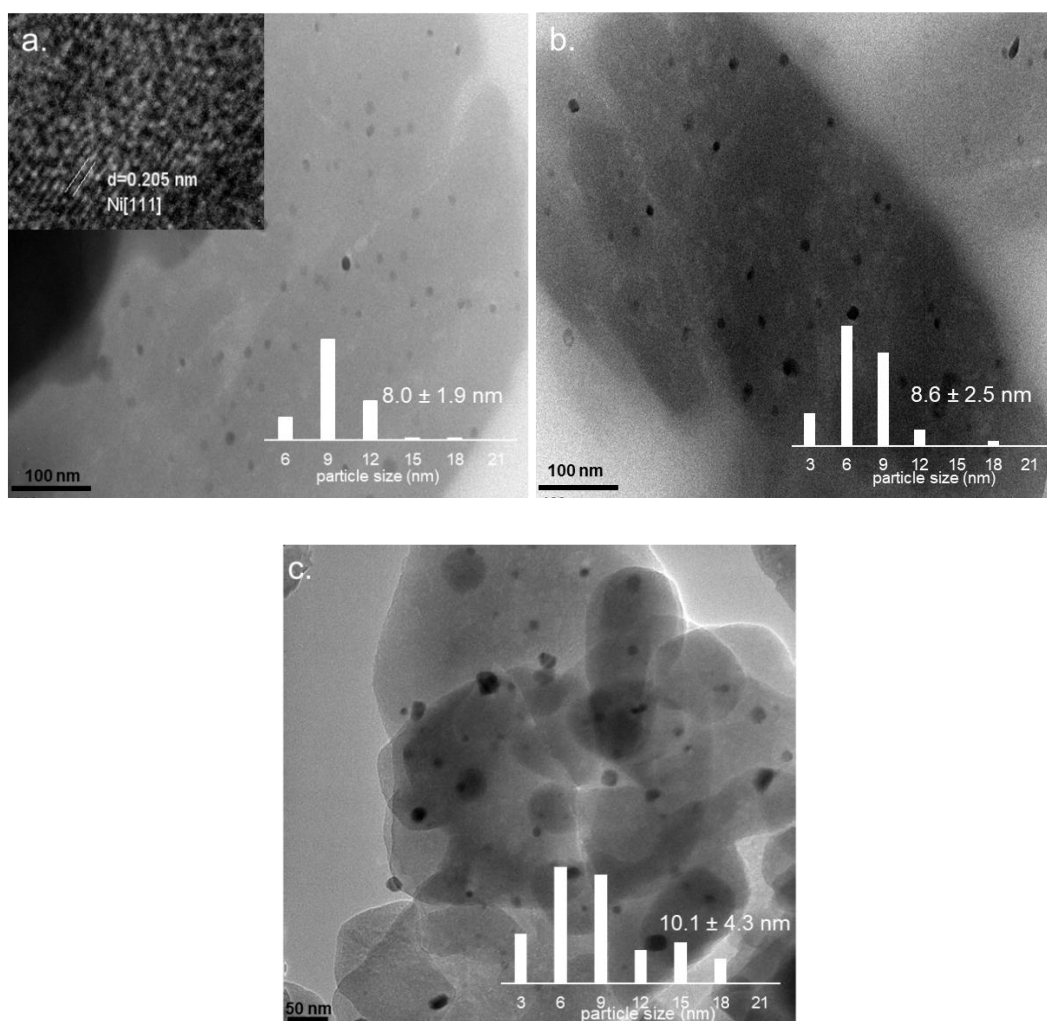


Figure 19. High Resolution TEM images and particle size distributions of (a) Ni-HMOR, (b) Ni-6MHMOR, and (c) Ni-13MHMOR

Dispersion and accessibility of Ni nanoparticles were investigated with CO-pulse chemisorption technique. All 3 previously reduced catalysts were exposed to CO pulses given through six port valve system at 40°C temperature. However, there were no observable change in between the areas obtained on mass spectroscopy even after 6 times of CO injections as seen in Figure 31. As a control experiment, similar experiments were carried out with Pt/TiO<sub>2</sub> and Ni impregnated HMOR. Both catalysts have 3% metal loading by weight. Ni impregnated HMOR again showed no chemisorption upon 6 consecutive CO pulse whereas Pt/TiO<sub>2</sub> showed observable CO chemisorption within first 2 CO pulse as it is seen in Figure 32. This experiment

revealed that with similar conditions CO chemisorption methods applied for Pt metals cannot be analogous to each other. CO pulse chemisorption studies generally conducted with materials with high Ni loadings such as 11% or more [71], [72]. Early studies on chemisorption of CO to reduced Ni surface was conducted Baker et.al at temperatures below 0 and room temperature under vacuum [95]. They proposed that CO adsorption to Ni surface is energetically more favorable than hydrogen adsorption on Ni surface. They also concluded that Ni adsorption at room temperature is not complete and CO adsorption on Ni is favored as the pressure increase and the temperature decrease. Yates and Garland also studied the CO adsorption on crystalline Ni surfaces by FTIR spectroscopy[96]. They also observed CO adsorption on Ni crystalline sites at considerably low pressure and it is defined as typical chemisorption. In addition, weak CO interaction was observed for dispersed and semicrystalline Ni species. There is still no certain pulse chemisorption technique on Ni in the literature. Different studies possess varying procedures and literature is not well agreement with each other yet. Delacruz et. al studied the effect of Ni carbonyl formation on catalyst deactivation and decomposition during the high temperature reduction of their Ni/ZrO<sub>2</sub> catalyst [97]. By looking at Ni crystalline size and content on ZrO<sub>2</sub>, they proposed a reduction mechanism in which volatile and mobile nickel carbonyl (Ni(CO)<sub>4</sub>) species formed and provided a decomposition of Ni content over zirconia support. The possibility of Ni dispersion by nickel carbonyl species could also be investigated for CO pulse chemisorption studies conducted on Ni catalysts at low temperatures to clarify the underlying mechanism of CO chemisorption on Ni surfaces.

### **4.3 Results of Aqueous-Phase HDC of TCE**

Aqueous phase reactions were carried out in a batch reactor at atmospheric pressure and room temperature. Activity of catalyst was first monitored by chloride ion selective electrode. 10 mg of reduced Ni-HMOR catalyst was loaded into reactor having 20 ppm TCE in 510 mL of deionized water (resitivity  $\approx 18\Omega.m$ ). Once the

reaction started Chloride concentration was monitored as in Figure 20. There was no observable chloride formation due to reaction product of HCl. However, Tarach et. al claimed almost 50% of conversion with Ni exchanged ZSM-5 and almost 70% of conversion with Ni exchanged SDUSY catalysts within 140 min [61]. Catalyst amount was  $2.3 \text{ mg L}^{-1}$  for Ni-SDUSY and  $3.5 \text{ mg L}^{-1}$  for Ni-ZSM-5. No chloride monitoring results was shared even though they have mentioned about they have used ISE for chloride monitoring. As a conclusion, study confusingly proposed both catalytic activity and adsorption mechanisms as an effective HDC paths.

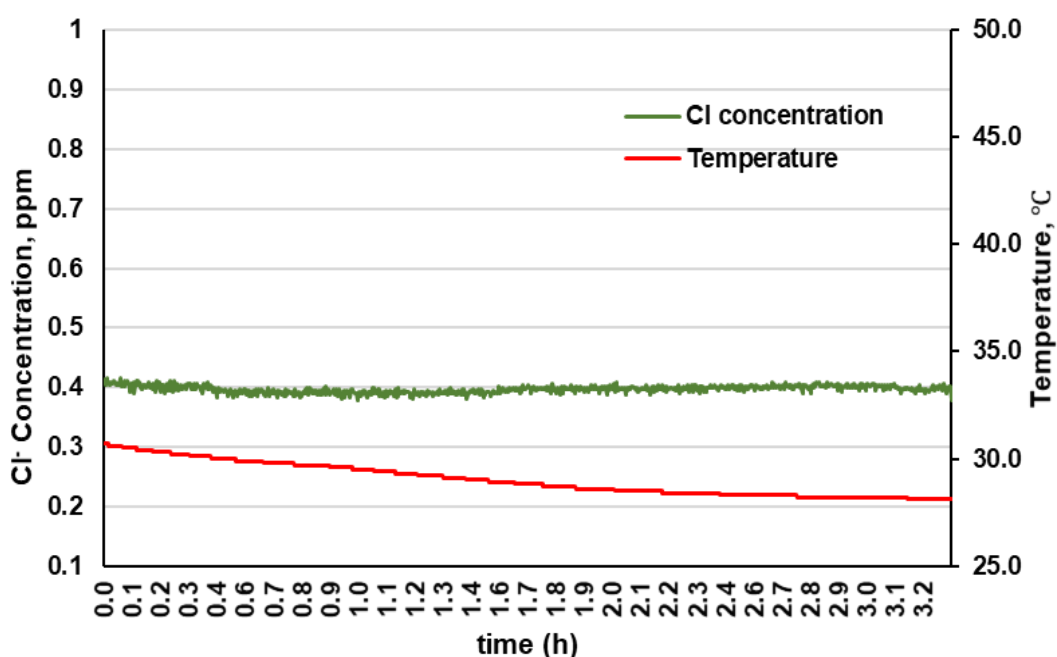


Figure 20.  $\text{Cl}^-$  concentration within the reactor with respect to time during the HDC of TCE with Ni-HMOR catalyst.

To understand the underlying mechanism clearly, reaction with Ni-HMOR was repeated to monitor reaction products with HPLC. Reactions were also carried out with Pd (1 wt%) / $\text{Al}_2\text{O}_3$  catalyst which is already proven to have an activity for aqueous phase HDC. Figure 21 and 22 represent the HPLC chromatographs of reaction samples taken from the reactor at certain time intervals. Retention time for TCE is 21 and 7 min for HCl. From the figure 22, it was clearly observed that HDC of TCE was almost completely over 18 h with Pd catalyst. Even the partially

chlorinated hydrocarbons and side products that could be visible in 2<sup>nd</sup> sample (15 min) went to complete reduction under hydrogen.

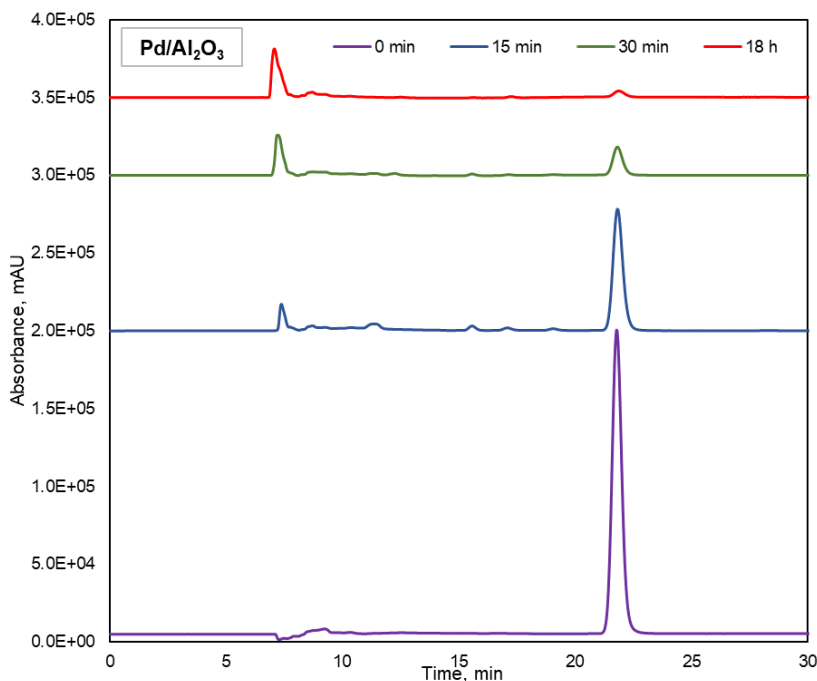


Figure 21. HPLC results of HDC with Pd/Al<sub>2</sub>O<sub>3</sub> catalyst.

On the other hand, Ni-HMOR could not reduce the TCE under hydrogenative environment at atmospheric conditions as shown by Figure 22. There is no increase in HCl peak and no considerable partially chlorinated hydrocarbons are available in the chromatographs of Ni-HMOR sample. These results suggested that Ni supported on zeolites have no noticeable activity towards HDC of TCE contrary to findings of Tarach et.al. Gas phase HDC of chlorinated hydrocarbons over Ni supported catalysts have been reported and reviewed in many studies [25], [38], [43], [64], [98]. Some studies reported Ni-Fe bimetallic nanoparticles had an activity towards HDC of TCE [99]. The synthesis and reduction procedures of nanoparticles should be considered carefully. Therefore, suggested catalytic activity on Ni exchanged zeolites by Tarach et.al should be reinvestigated to clarify the points between the physical adsorption and kinetic phenomena.

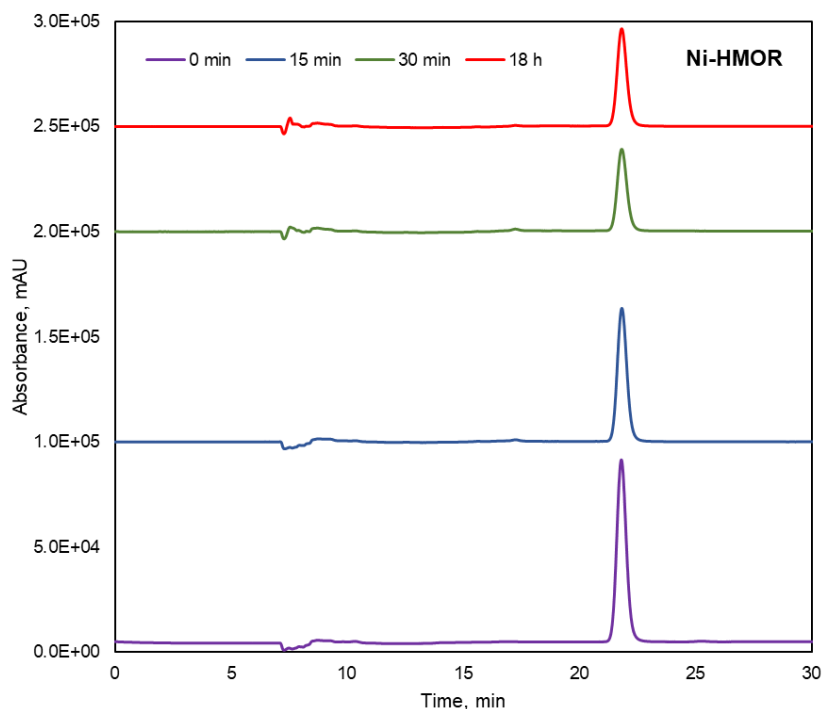


Figure 22. HPLC results of HDC with Ni-HMOR catalyst.

#### 4.4 Results of Gas-phase HDC of TCE

Gas-phase catalytic HDC tests were conducted at 300 °C with 30 mg of catalyst providing differential reactor element analysis. Each catalyst was reduced prior to reaction under pure hydrogen. Used catalysts were collected for further post-reaction analysis with TGA.

The catalytic conversions of three catalysts with respect to time are given in Figure 18. As it is shown in the Figure 23, the highest catalytic conversion was obtained with the Ni-6MHMOR sample with an initial TCE conversion of 33.9%. 28.3% of initial TCE conversion was obtained with the Ni-13MHMOR; the lowest initial TCE conversion of 14.4%, was acquired with the Ni-HMOR sample. Percent conversion losses were also obtained as tabulated in Table 6. Regarding conversion loss, the Ni-HMOR sample with the lowest activity also performs the highest conversion loss of 42%. The lowest conversion loss of 27% after almost 6 h of reaction was observed

with the Ni-6MHMOR. Despite the different conversion trends performed by the 3 catalysts, product selectivity distributions trends have shown very similar product distribution and selectivity as presented in Table 7. The very broad product distribution was observed from methane, ethylene, ethane, propylene, and C4 compounds to other chlorinated hydrocarbons. TCE was mostly converted to ethylene and propylene rather than ethane with all three catalysts with an H<sub>2</sub>:TCE ratio of ~60:1. Same product distribution and selectivity suggest that the reaction mechanism is almost the same for all three of the catalysts. However, catalytic performance is altered the most with moderate (6 M) acid treatment. Figure 18 demonstrated that there were Ni species reduced by H<sub>2</sub> within the broad temperature range (600 °C to 900 °C) giving maxima around 800 °C. To understand whether the Ni-HMOR sample could be reduced completely prior to the reaction, the reaction was repeated with 3 h of pre-reduction, and an identical activity result was obtained with Ni-HMOR as in Figure 24. Reactions were also repeated with H<sub>2</sub>:TCE of 10-15 and all three catalysts were almost deactivated within 200 minutes as shown in Figure 26. Figure 27 represents the selectivity trends which were also similar to excess H<sub>2</sub> conditions up to 100 minutes where the catalytic activity is still considerably high giving conversions higher than 2%. In figure 28, no considerable background activity has been observed over HMOR and 6MHMOR supports. However, HMOR represented more activity compared to 6MHMOR. A similar situation was also observed by Srebowata et.al. with zeolite-beta (BEA) where bare BEA gave almost 10% dichloroethane conversion to vinyl chloride whereas dealuminated BEA gave almost no conversion [38]. This was attributed to strong Bronsted acids in bare BEA, which HMORs have as in Figure 15a. TCE adsorption affinity has been reported to increase over different zeolite surfaces with increasing Si/Al ratio due to increasing hydrophobicity by experimental and theoretical studies[34], [65], [100], [101]. Acid modification of the support can alter the catalytic performance up to some extent by strong acid site extraction. However, the 13MHMOR sample performed less activity in terms of TCE conversion. Chintawar et.al. suggested that Si-OH groups are responsible for TCE adsorption by FTIR

studies and as the Si/Al goes to infinity surface interactions were proposed to occur by pore filling process and by van der Waals forces rather than strong chemical interactions proposed by the sorbent [65]. This could be another reason for the Ni-13MHMOR sample to have lower activity compared to Ni-6MHMOR.

The metal loadings of all three catalysts are similar, with slight differences as presented in Table 4. However, the variations in catalytic activity are not directly correlated with the metal loading. This is evident from the activity per Ni weight percentage calculated for each catalyst, as shown in Table 6. According to Ni content, the catalyst Ni-6MHMOR and Ni-13MHMOR samples perform a close activity trend. The conversion loss of the Ni-6MHMOR sample is very close to the Ni-13MHMOR suggesting the modified acidity by dealumination contributes to the deactivation of Ni-exchanged MORs but the degree of dealumination affects the conversion loss up to some extent. In other words, the higher the Si/Al ratio of the zeolite higher the conversion loss of the catalyst is. This could be a result of chloride poisoning of metal Ni species due to high HCl formation consequent to high conversions. Chloride poisoning is found to be more likely on Al-rich Ni-BEA for HDC of TCE by post-H<sub>2</sub>-TPD on the used catalyst [64]. However, they also reported almost the same HCl formation for both Si and Al-rich Ni-BEAs after HDC of dichloroethane [38]. For both cases, it should be considered catalysts' activities towards TCE and DCE are different resulting in different product distribution and mechanisms. It is also reported that the higher the hydrophilicity of the support it will be more prone to concentrate these Cl<sup>-</sup> in the absence of active metal [55]. However, Cl<sup>-</sup> ions are generally suggested to be attracted by active metal phases [55], [63], [102]. This could be again caused by the strong acid sites composed over the zeolite surfaces as shown by pyridine adsorption in Figure 15a.

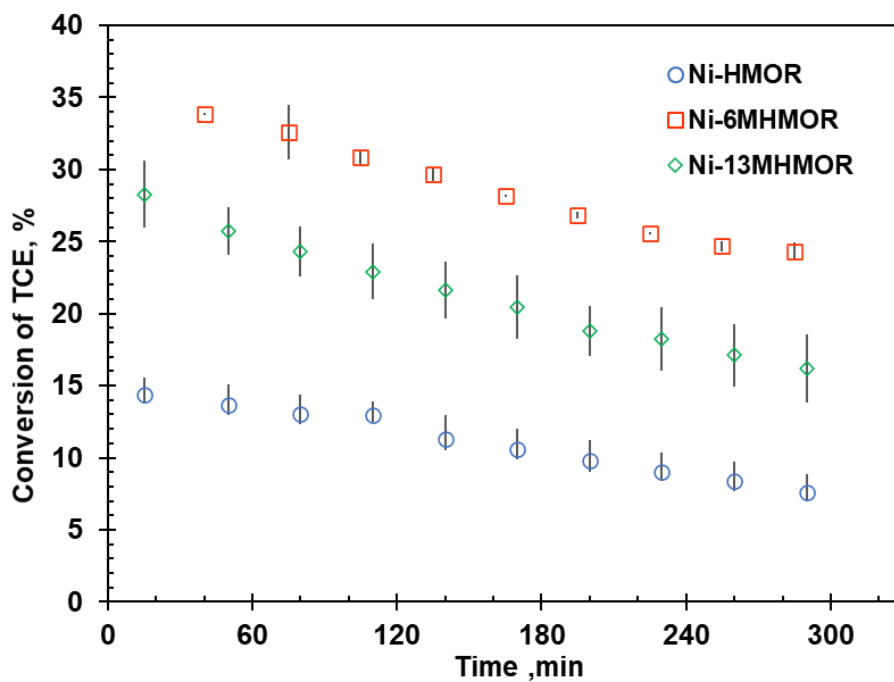


Figure 23. TCE conversion of Ni exchanged XMHMORs with respect to time at 300 °C, 1 atm and H<sub>2</sub>:TCE~60:1.

Table 6. Tabulated HDC activity results of Ni exchanged XMHMORs at 300 °C, 1 atm and H<sub>2</sub>:TCE~60:1.

Catalyst	Rate of % conversion loss (X%/min)	% Conversion loss	Ni wt%	Initial conversion factor per Ni
Ni-HMOR	0.023	42	0.45	30.4
Ni-6MHMOR	0.036	27	0.61	56.5
Ni-13MHMOR	0.041	37	0.52	54.4

Table 7. Tabulated product distributions over Ni exchanged XMHMORs at 300 °C, 1 atm and H<sub>2</sub>:TCE~60:1.

	Ni-HMOR	Ni-6MHMOR	Ni-13MHMOR
<b>Methane</b>	7.7	7.5	7.7
<b>Ethylene</b>	51.8	49.4	48.5
<b>Ethane</b>	2.0	2.1	2.1
<b>Propylene</b>	27.3	29.8	29.7
<b>C4s</b>	8.0	7.7	8.7
<b>Chlorinated HCs</b>	3.1	3.5	3.3

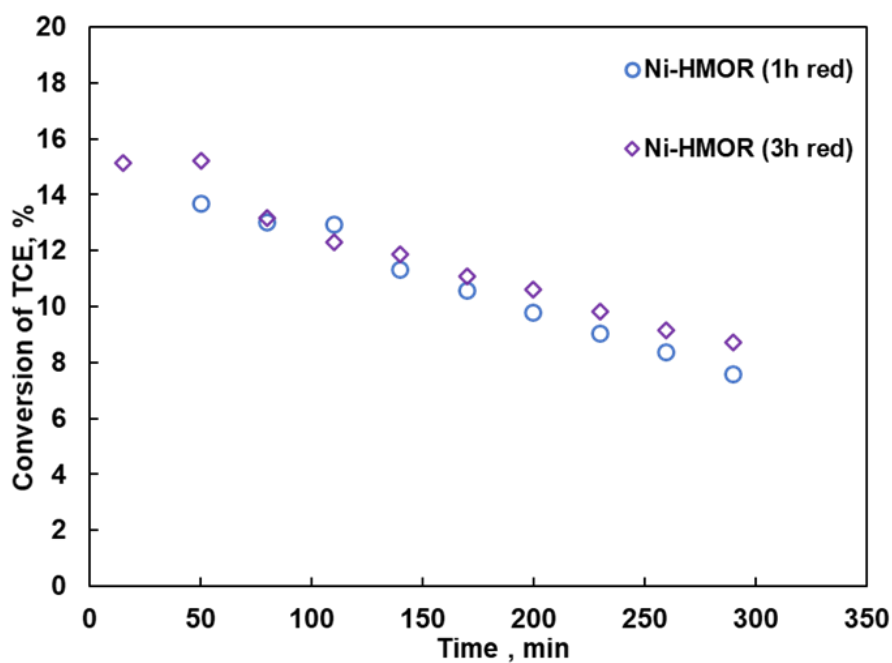


Figure 24. TCE conversion of bare Ni-HMORs with respect to time at 300 °C, 1 atm and H<sub>2</sub>:TCE~60:1 with different pre-reduction times.

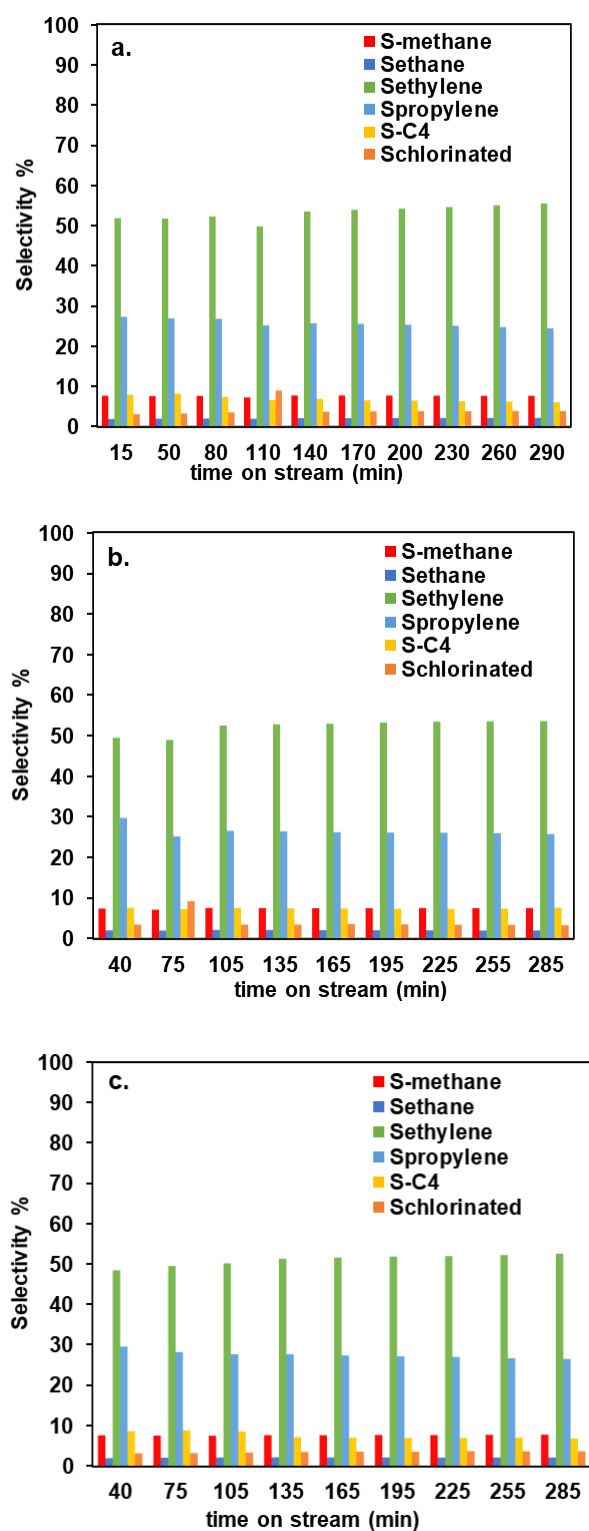


Figure 25. Product selectivity distributions with respect to time of 3 different catalysts a) Ni-HMOR b) Ni-6MHMOR and c) Ni-13MHMOR at 300 °C, 1 atm and H<sub>2</sub>:TCE~60:1.

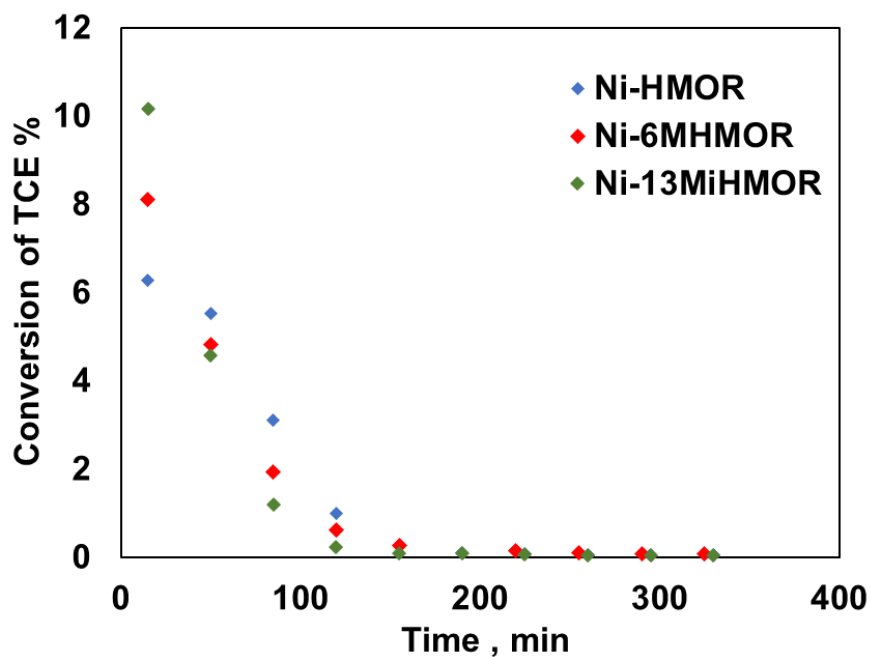


Figure 26. TCE conversion of Ni exchanged XMHMORs with respect to time at 300 °C, 1 atm with H<sub>2</sub>:TCE~13.

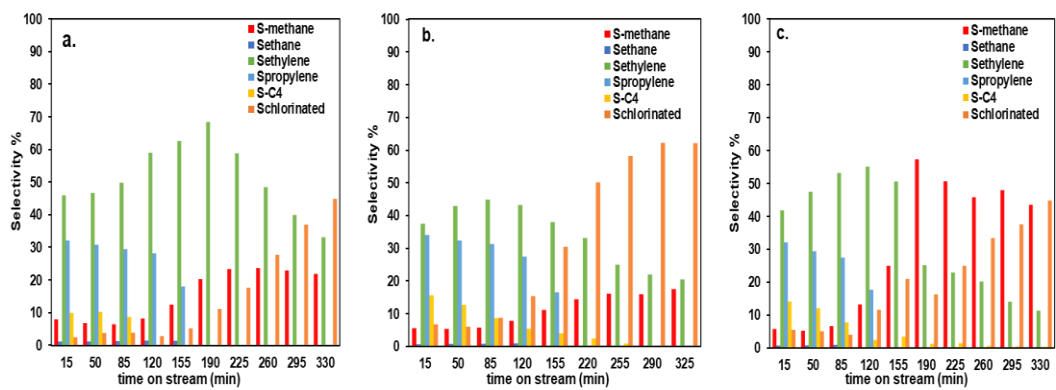


Figure 27. Selectivity product distributions with respect to time of 3 different catalysts a) Ni-HMOR b) Ni-6MHMOR and c) Ni-13MHMOR at 300 °C, 1 atm and H<sub>2</sub>:TCE~13.

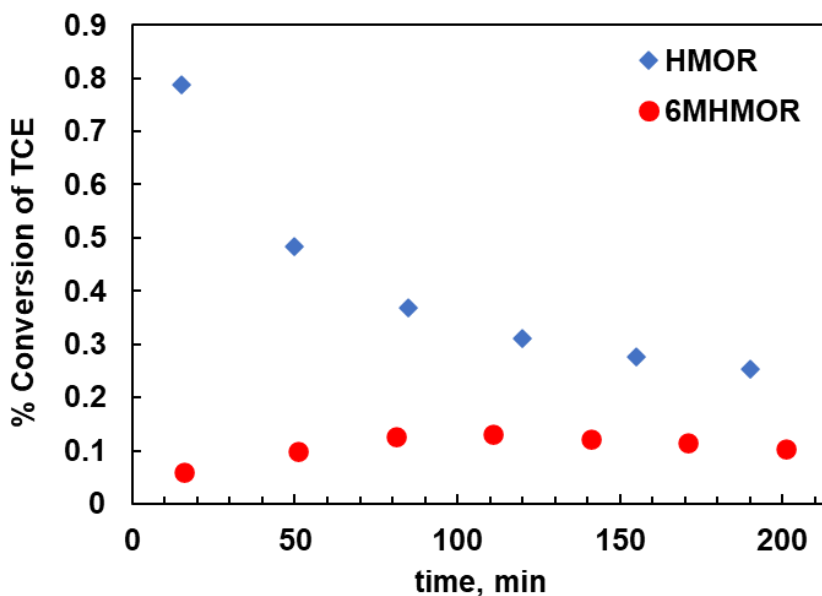


Figure 28. Background activity of HMOR (bare) and 6MHMOR (dealuminated) supports at 300 °C, 1 atm and H<sub>2</sub>:TCE~60:1.

## 4.5 Post-Reaction Analysis of Used Catalysts

### 4.5.1 Thermogravimetric Analysis of Used Catalysis

Used catalysts were examined by TGA analysis to understand the deactivation of the catalyst after HDC activity tests. Figure 29 demonstrates the rate of mass loss with respect to rising temperature for all 3 catalysts in an oxygenating environment. Under the reaction conditions, a significant extent of carbon formation was not observed, as shown by thermogravimetric analysis over the used samples. The first peak around 80-100 °C corresponds to TCE and physisorbed water on the samples. However, the TGA profile of used catalysts shows that the highest amount of carbonaceous deposit was observed over Ni supported on bare mordenite in between the 400 °C - 600 °C. Relatively low amount of carbonaceous deposition is observed for Ni-6MMHOR whereas no carbonaceous deposit over Ni-13MHMOR were observed as in Figure 29. This shows that as the degree of dealumination increased

tolerance of carbonaceous deposition also increases over the catalyst. This could be mainly attributed to the loss of strong BAS. It is also known that strong acid sites are considered as coking agents. The formation of less carbonaceous species over the dealuminated catalysts for HDC reactions was in line with the literature [38], [64].

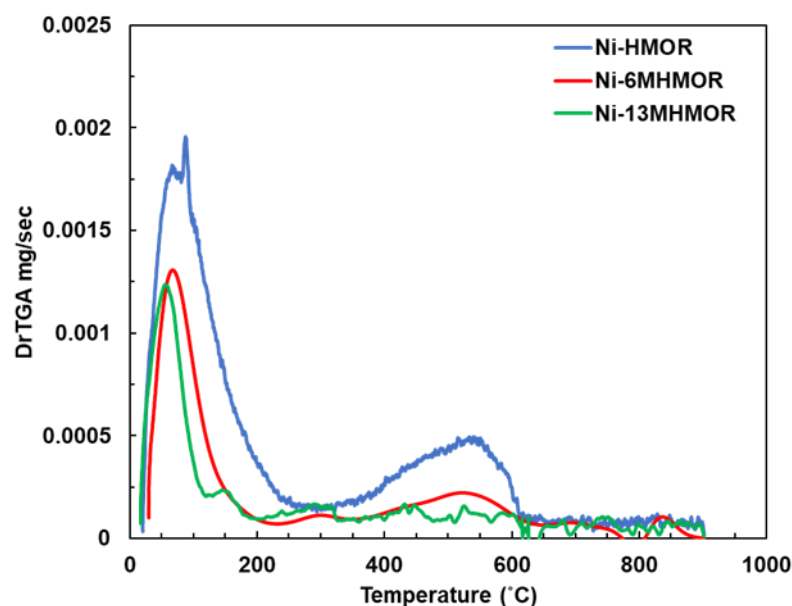


Figure 29. TGA results of HDC-tested Ni-XMHMORs, 300°C, 1 atm and H<sub>2</sub>:TCE~60:1.

#### 4.5.2 Temperature Programmed Hydrogenation of Used Catalysts

TPH experiments were conducted successfully as described in experimental section. Figure 30 demonstrates the HCl and CH<sub>4</sub> signals collected during hydrogenation of all 3 used catalysts. To chase the HCl formation during hydrogenation m/z of 36 and 38 signals were chased for all 3 samples. 36 signal is the strongest signal for HCl whereas 38 is relatively weaker. m/z=38 is also a signal for hydrocarbons like propane, propylene, butane and butene. In Figure 30a, there are no formation of HCl during the entire TPH. However, in Figure 30c, there is considerable change for Ni-HMOR sample. Thus, coinciding trend in 36 signal can be attributed to formation of hydrocarbons upon hydrogenation since methane formation was also observed at

those temperature. Oligomerization of methane to propane, butane etc. under pure hydrogen atmosphere at elevated temperature is also possible. TPH studies were also demonstrated by Srebowata et.al. during the hydrodechlorination trichloroethylene and dichloroethane with Ni impregnated and dealuminated beta (BEA) zeolites[38], [64]. They observed high HCl formation during TPH for bare Ni-BEA after HDC of TCE. On the other hand, dealuminated Ni-BEA also showed less HCl formation at elevated temperatures. For the HDC of TCE, however, almost same amount of HCl formation observed and they concluded that HCl formation is independent of dealumination of support. Their conclusions in two different study are contradictory and not clarified very well. It should also be noted that their reaction time is around 1000 min which is almost 3 times longer than our reaction time. Figure 30 b also showed the methane formation during the TPH. All 3 samples showed slight methane formation around 500 °C but Ni-HMOR sample provided a considerably high methane formation around 800 °C. This can contribute to strong acid sites confined in bare MOR support. Strong acid sites promote strongly bounded carbon deposition on zeolite support. Srebowata et.al. also observed high methane formation with bare BEA support whereas negligible formation of methane formed upon catalyst supported with dealuminated BEA[38], [64]. There were no changes upon water signals ( $m/z=17, 18$ ).  $m/z=15$  and  $12$  signals are analogous to  $16$  signal as shown in Figure 30b.

Chloride poisoning affect on catalyst was also investigated by XPS analysis. After HDC at 300°C and 1 atm with  $H_2:TCE\sim 60:1$  on Ni-HMOR, catalyst sample was analyzed by XPS. Results were given in Appendix C. Figure 33 and 34 represents raw and deconvoluted data of certain elements respectively. Unfortunately, no clear Ni binding energy observations was accomplished due to very low Ni loadings. Figure 34 represents Cl  $2p_{3/2}$  and  $2p_{1/2}$ . Binding energy for Ni shifted to 200 eV which corresponds to Cl atom coming from chlorinated hydrocarbons such as TCE [103]. Since no nickel is observed in Ni  $2p$  region, it was expected to observe no shift in Cl towards  $NiCl_2$  region which generally corresponds to 198 eV. Deconvoluted Al and C peaks possessed no shift towards chloride bounded regions.

Higher Ni loadings is required to observe Ni-Cl formations due to the quantitative limitations of XPS.

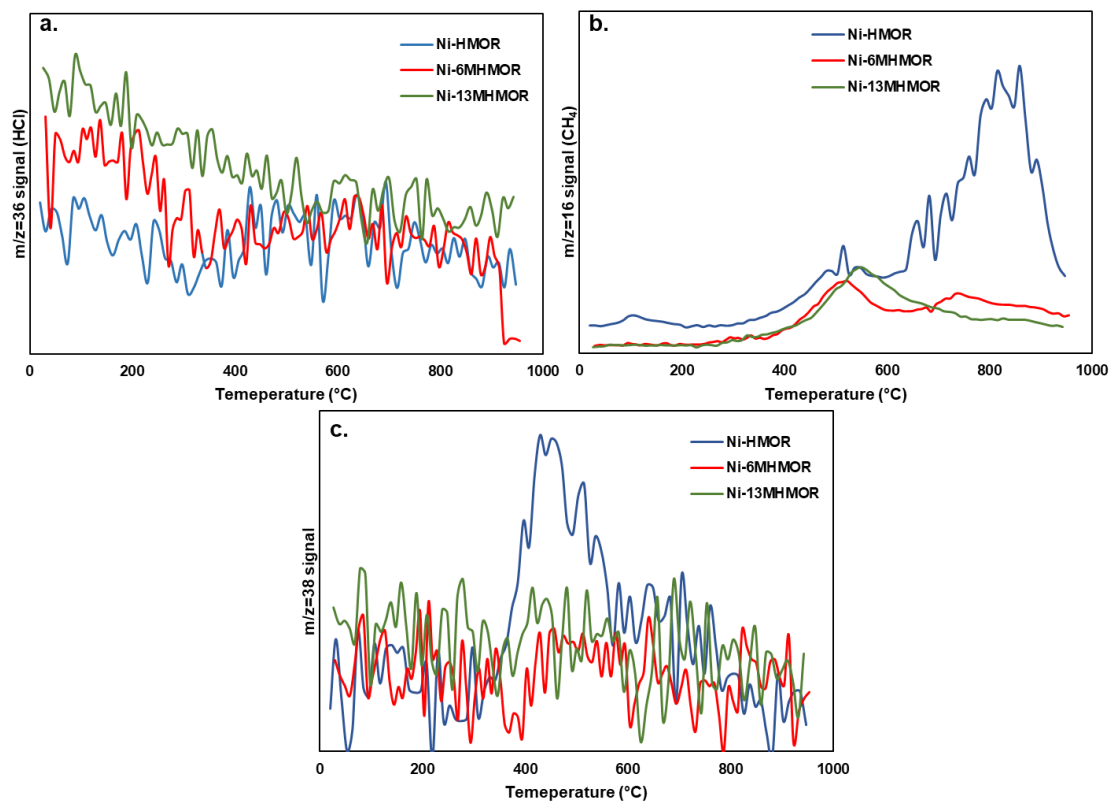


Figure 30. TPD of used catalysts, represents (a) the  $m/z=36$  signal of HCl, (b) the  $m/z=16$  signal of CH<sub>4</sub> and (c) the  $m/z=38$  signal with respect to increasing temperature.



## CHAPTER 5

### CONCLUSIONS

In this study, dealuminated and nickel exchanged mordenites have been synthesized, characterized from various aspects and tested for catalytic hydrodechlorination of trichlorethylene.

As a catalyst support zeolite with a mordenite framework type was successfully modified without the destruction of the structure upon 6 M and 13 M nitric acid treatments. BET results showed that dealuminated MORs preserved their microporous structure very well upon dealumination when the t-plot micropore and BET surface areas compared for each sample. XRD results also confirmed structural preservation after dealumination. Crystal sizes of 13MHMOR support decreased upon dealumination compared to HMOR and 6MHMOR due to severity of acid treatment and major elemental change within the zeolite structure. Si/Al ratios were obtained as 9.6, 58.3 and 101.4 for HMOR, 6MHMOR and 13MHMOR samples respectively demonstrating linear relation with the degree of dealumination. In-situ DRIFTS of adsorbed pyridine on different temperatures demonstrated the presence of strong bronsted acid sites at  $1541\text{cm}^{-1}$  and  $1486\text{cm}^{-1}$  was no longer observable as the degree of acid treatment increased. Number of BAS acid sites at  $1590\text{cm}^{-1}$  increased due to the silanol nests formed upon strong dealumination. However, the strength of these sites is again decreased upon dealumination as shown by pyridine TPD.

Bare and dealuminated supports successfully loaded with nickel via ion exchange method. There is no significant variance in nickel loading considering the Ni weight percentages obtained as 0.45, 0.6, and 0.52 for bare, 6 M and 13 M dealuminated samples respectively. Reduction profiles of dealuminated catalyst showed almost similar profiles upon H<sub>2</sub>-TPR where major reduction occurred at 650 °C for catalysts with dealuminated supports whereas catalyst supported on bare support

demonstrated a major reduction peak around 850 °C which can be related to the more stably exchanged Ni cations within the zeolite cages. H<sub>2</sub> reduction prior to HDC reaction resulted in inevitable Ni agglomeration of exchanged cations and nickel constituents upon zeolite internal and external surfaces. This effect was confirmed with HR-TEM analysis where nickel nanoparticles were observed with an average particle sizes of 8±1.9 nm, 8.6±2.5 and 10.1±4.3 for Ni-HMOR, Ni-Ni-6MHMOR and Ni-13MHMOR catalysts respectively. TEM images also confirmed that the nickel particle sizes and distributions were almost in the similar range for all three catalysts.

In terms of catalytic activity, all 3 catalysts were firstly tested with aqueous phase batch reactor. However, no appreciable activity with Ni supported catalysts were observed by monitoring the reaction products with an ion selective electrode and HPLC.

Ni-6MHMOR showed the best performance during the gas-phase catalytic activity tests at 300 °C and 1 atm in excess H<sub>2</sub> environment over approximately 300 minutes with minimum percent conversion loss. Similar selectivity trends and similar product distributions suggested similar reaction mechanisms for all 3 catalysts.

Post reaction analysis with TGA demonstrated highest carbonaceous deposition Ni-HMOR catalyst which could be attributed to the strong and stable acid sites confined in zeolite framework whereas the delaminated samples had shown comparably less amount carbonaceous formation. TPH experiments also suggested the highest carbonaceous deposition over Ni-HMOR which are analogous to TGA analysis. No certain HCl formation is observed over TPH experiments due to low amount of Ni loadings.

All in all, optimized acidity of the catalyst support has been demonstrated to be an essential factor enhancing the HDC performance of the catalyst in terms of conversion and deactivation.

## REFERENCES

- [1] W. Liu, L. Chen, X. Liu, J. Chen, R. Liu, and H. Niu, "Comparison of the health risks associated with different exposure pathways of multiple volatile chlorinated hydrocarbons in contaminated drinking groundwater," *Environmental Pollution*, vol. 255, Dec. 2019, doi: 10.1016/j.envpol.2019.113339.
- [2] B. Huang, C. Lei, C. Wei, and G. Zeng, "Chlorinated volatile organic compounds (Cl-VOCs) in environment - sources, potential human health impacts, and current remediation technologies," *Environment International*, vol. 71. Elsevier Ltd, pp. 118–138, 2014. doi: 10.1016/j.envint.2014.06.013.
- [3] P. J. Squillace and C. V. Price, "NATIONAL WATER-QUALITY ASSESSMENT PROGRAM," 1996.
- [4] WHO, "Guidelines for Drinking-water Quality FOURTH EDITION INCORPORATING THE FIRST ADDENDUM," 2017.
- [5] K. E. Knox, R. E. Dodson, R. A. Rudel, C. Polsky, and M. R. Schwarzman, "Identifying Toxic Consumer Products: A Novel Data Set Reveals Air Emissions of Potent Carcinogens, Reproductive Toxicants, and Developmental Toxicants," *Environ Sci Technol*, vol. 57, no. 19, pp. 7454–7465, May 2023, doi: 10.1021/acs.est.2c07247.
- [6] I. Rusyn, W. A. Chiu, L. H. Lash, H. Kromhout, J. Hansen, and K. Z. Guyton, "Trichloroethylene: Mechanistic, epidemiologic and other supporting evidence of carcinogenic hazard," *Pharmacology and Therapeutics*, vol. 141, no. 1. pp. 55–68, Jan. 2014. doi: 10.1016/j.pharmthera.2013.08.004.
- [7] "National Primary Drinking Water Regulations : EPA 816-F-09-004, in: U.S.E.P. Agency (Ed.)," 2009.

- [8] EPA, “Ground Water and Drinking Water: National Primary Drinking Water Regulations,” 2023. <https://www.epa.gov/ground-water-and-drinking-water/national-primary-drinking-water-regulations>
- [9] D. Wartenberg, D. Reyner, and C. S. Scott<sup>2</sup>, “Trichloroethylene and Cancer: Epidemiologic Evidence.”
- [10] P. I. Beamer, C. E. Luik, L. Abrell, S. Campos, M. E. Martínez, and A. E. Sáez, “Concentration of trichloroethylene in breast milk and household water from Nogales, Arizona,” *Environ Sci Technol*, vol. 46, no. 16, pp. 9055–9061, Aug. 2012, doi: 10.1021/es301380d.
- [11] “ATSDR Substance Priority List (SPL) and Completed Exposure Pathway (CEP) Report Data through 2019,” 2019. [Online]. Available: [www.atsdr.cdc.gov/SPL](http://www.atsdr.cdc.gov/SPL)
- [12] ATSDR Case Studies in Environmental Medicine, “Trichloroethylene Toxicity,” 2022.
- [13] “European Union Risk Assessment Report Trichloroethylene,” 2004.
- [14] Agency for Toxic Substances and Disease Registry, “Toxicological Profile for Trichloroethylene,” 2019.
- [15] U.S. EPA., “Toxicity and exposure assessment for children’s health. Trichloroethylene — TEACH chemical summary.,” 2007. [Online]. Available: <http://www.epa.gov/teach/>.
- [16] H. H. Russell, J. E. Matthews, G. W. Sewell, R. S. Kerr Environmental, and W. W. Kovalick, “Ground Water Issue EPA TCE Removal from Contaminated Soil and Ground Water Superfund Technology Support Center for Ground Water,” 1992.
- [17] World Health Organization, “WHO guidelines for indoor air quality : selected pollutants,” 2010. [Online]. Available: [www.euro.who.int](http://www.euro.who.int)

- [18] Z. Zhao, Y.-L. Fang, P. J. J. Alvarez, and M. S. Wong, "Degrading perchloroethene at ambient conditions using Pd and Pd-on-Au reduction catalysts," *APPLIED CATALYSIS B-ENVIRONMENTAL*, vol. 140, pp. 468–477, 2013, doi: 10.1016/j.apcatb.2013.04.032.
- [19] M. R. Flid, L. M. Kartashov, and Y. A. Treger, "Theoretical and Applied Aspects of Hydrodechlorination Processes-Catalysts and Technologies," *CATALYSTS*, vol. 10, no. 2, 2020, doi: 10.3390/catal10020216.
- [20] C. Dai *et al.*, "Current progress in remediation of chlorinated volatile organic compounds: A review," *Journal of Industrial and Engineering Chemistry*, vol. 62, pp. 106–119, Jun. 2018, doi: 10.1016/j.jiec.2017.12.049.
- [21] A. Elola, E. Díaz, and S. Ordoñez, "A new procedure for the treatment of organochlorinated off-gases combining adsorption and catalytic hydrodechlorination," *Environ Sci Technol*, vol. 43, no. 6, pp. 1999–2004, Mar. 2009, doi: 10.1021/es803226v.
- [22] B. P. Chaplin *et al.*, "Critical review of Pd-based catalytic treatment of priority contaminants in water," *Environmental Science and Technology*, vol. 46, no. 7, pp. 3655–3670, Apr. 03, 2012. doi: 10.1021/es204087q.
- [23] G. V Lowry and M. Reinhard, "Hydrodehalogenation of 1- to 3-Carbon Halogenated Organic Compounds in Water Using a Palladium Catalyst and Hydrogen Gas," *Environ Sci Technol*, vol. 33, no. 11, pp. 1905–1910, 1999, doi: 10.1021/es980963m.
- [24] C. Schüth, S. Disser, F. Schüth, and M. Reinhard, "Tailoring catalysts for hydrodechlorinating chlorinated hydrocarbon contaminants in groundwater," 2000.
- [25] M. A. Keane, "Supported Transition Metal Catalysts for Hydrodechlorination Reactions," *ChemCatChem*, vol. 3, no. 5, pp. 800–821, May 09, 2011. doi: 10.1002/cctc.201000432.

- [26] H. Sohn *et al.*, “Effect of high-temperature on the swellable organically-modified silica (SOMS) and its application to gas-phase hydrodechlorination of trichloroethylene,” *Appl Catal B*, vol. 209, pp. 80–90, 2017, doi: 10.1016/j.apcatb.2017.02.056.
- [27] M. S. Wong *et al.*, “Cleaner water using bimetallic nanoparticle catalysts,” *JOURNAL OF CHEMICAL TECHNOLOGY AND BIOTECHNOLOGY*, vol. 84, no. 2, pp. 158–166, 2009, doi: 10.1002/jctb.2002.
- [28] G. Yuan and M. A. Keane, “Catalyst deactivation during the liquid phase hydrodechlorination of 2,4-dichlorophenol over supported Pd: Influence of the support,” in *Catalysis Today*, Dec. 2003, pp. 27–36. doi: 10.1016/j.cattod.2003.08.004.
- [29] G. V Lowry and M. Reinhard, “Pd-Catalyzed TCE Dechlorination in Groundwater: Solute Effects, Biological Control, and Oxidative Catalyst Regeneration,” *Environ Sci Technol*, vol. 34, no. 15, pp. 3217–3223, 2000, doi: 10.1021/es991416j.
- [30] D. Comandella, S. Wosidlo, A. Georgi, F. D. Kopinke, and K. Mackenzie, “Efforts for long-term protection of palladium hydrodechlorination catalysts,” *Appl Catal B*, vol. 186, pp. 204–211, Jun. 2016, doi: 10.1016/j.apcatb.2015.12.043.
- [31] G. Celik *et al.*, “Swelable Organically Modified Silica (SOMS) as a Catalyst Scaffold for Catalytic Treatment of Water Contaminated with Trichloroethylene,” *ACS Catal*, vol. 8, no. 8, pp. 6796–6809, Aug. 2018, doi: 10.1021/acscatal.8b01700.
- [32] G. Celik, S. A. Ailawar, S. Gunduz, J. T. Miller, P. L. Edmiston, and U. S. Ozkan, “Aqueous-phase hydrodechlorination of trichloroethylene over Pd-based swellable organically-modified silica (SOMS): Catalyst deactivation due to chloride anions,” *Appl Catal B*, vol. 239, 2018, doi: 10.1016/j.apcatb.2018.08.065.

- [33] G. Celik, S. A. Ailawar, S. Gunduz, J. T. Miller, P. L. Edmiston, and U. S. Ozkan, "Aqueous-Phase Hydrodechlorination of Trichloroethylene over Pd-Based Swellable Organically Modified Silica: Catalyst Deactivation Due to Sulfur Species," *Ind Eng Chem Res*, vol. 58, no. 10, 2019, doi: 10.1021/acs.iecr.8b05979.
- [34] H. Cheng and M. Reinhard, "Sorption of trichloroethylene in hydrophobic micropores of dealuminated Y zeolites and natural minerals," *Environ Sci Technol*, vol. 40, no. 24, pp. 7694–7701, Dec. 2006, doi: 10.1021/es060886s.
- [35] M. L. Brusseau and R. M. Maier, "SOIL AND GROUNDWATER REMEDIATION," 2004.
- [36] D. Basu, S. Ailawar, G. Celik, P. Edmiston, and U. S. Ozkan, "Effect of High Temperature on Swellable Organically Modified Silica (SOMS) and Its Application for Preferential CO Oxidation in H<sub>2</sub> Rich Environment," *ChemCatChem*, vol. 12, no. 14, pp. 3753–3768, Jul. 2020, doi: 10.1002/cctc.202000397.
- [37] X. Ning, Y. Sun, H. Fu, X. Qu, Z. Xu, and S. Zheng, "N-doped porous carbon supported Ni catalysts derived from modified Ni-MOF-74 for highly effective and selective catalytic hydrodechlorination of 1,2-dichloroethane to ethylene," *Chemosphere*, vol. 241, Feb. 2020, doi: 10.1016/j.chemosphere.2019.124978.
- [38] A. Śrebawata, R. Baran, D. Łomot, D. Lisovytskiy, T. Onfroy, and S. Dzwigaj, "Remarkable effect of postsynthesis preparation procedures on catalytic properties of Ni-loaded BEA zeolites in hydrodechlorination of 1,2-dichloroethane," *Appl Catal B*, vol. 147, pp. 208–220, Apr. 2014, doi: 10.1016/j.apcatb.2013.08.040.
- [39] I. I. Kamińska *et al.*, "Batch and flow hydrotreatment of water contaminated by trichloroethylene on active carbon supported nickel catalysts," *Appl Catal A Gen*, vol. 582, Jul. 2019, doi: 10.1016/j.apcata.2019.117110.

- [40] J. Cejka, H. Van Bekkum, A. Corma, and F. Schüth, “Studies in Surface Science and Catalysis 168: Introduction to Zeolite science and practice,” *Studies in Surface Science and Catalysis*. 2007. doi: 10.1016/S0167-2991(07)80803-2.
- [41] X. Jia, W. Khan, Z. Wu, J. Choi, and A. C. K. Yip, “Modern synthesis strategies for hierarchical zeolites: Bottom-up versus top-down strategies,” *Advanced Powder Technology*, vol. 30, no. 3. Elsevier B.V., pp. 467–484, Mar. 01, 2019. doi: 10.1016/j.appt.2018.12.014.
- [42] D. Kerstens, B. Smeyers, J. Van Waeyenberg, Q. Zhang, J. Yu, and B. F. Sels, “State of the Art and Perspectives of Hierarchical Zeolites: Practical Overview of Synthesis Methods and Use in Catalysis,” *Advanced Materials*, vol. 32, no. 44. Wiley-VCH Verlag, Nov. 01, 2020. doi: 10.1002/adma.202004690.
- [43] S. Ordóñez, H. Sastre, and F. V Díez, “Hydrodechlorination of aliphatic organochlorinated compounds over commercial hydrogenation catalysts,” 2000.
- [44] L. A. Pretzer *et al.*, “Hydrodechlorination catalysis of Pd-on-Au nanoparticles varies with particle size,” *J Catal*, vol. 298, pp. 206–217, Feb. 2013, doi: 10.1016/j.jcat.2012.11.005.
- [45] T. Li, X. Li, Y. Teng, H. Wang, and H. Sun, “Phosphidation of microscale zero-valent iron (P-mZVI) for enhanced dechlorination of trichloroethylene,” *J Clean Prod*, vol. 386, Feb. 2023, doi: 10.1016/j.jclepro.2022.135803.
- [46] S. Ordóñez, F. V Díez, and H. Sastre, “Characterisation of the deactivation of platinum and palladium supported on activated carbon used as hydrodechlorination catalysts,” 2001.
- [47] S. Ordóñez, H. Sastre, and F. V Díez, “Hydrodechlorination of tetrachloroethene over Pd/Al<sub>2</sub>O<sub>3</sub>: influence of process conditions on catalyst performance and stability,” 2003.

- [48] J. Deng *et al.*, “Generation of atomic hydrogen by Ni-Fe hydroxides: Mechanism and activity for hydrodechlorination of trichloroethylene,” *Water Res*, vol. 207, Dec. 2021, doi: 10.1016/j.watres.2021.117802.
- [49] S. De Corte *et al.*, “Biosupported bimetallic Pd-Au nanocatalysts for dechlorination of environmental contaminants,” *Environ Sci Technol*, vol. 45, no. 19, pp. 8506–8513, Oct. 2011, doi: 10.1021/es2019324.
- [50] M. O. Nutt, K. N. Heck, P. Alvarez, and M. S. Wong, “Improved Pd-on-Au bimetallic nanoparticle catalysts for aqueous-phase trichloroethene hydrodechlorination,” *APPLIED CATALYSIS B-ENVIRONMENTAL*, vol. 69, no. 1–2, pp. 115–125, 2006, doi: 10.1016/j.apcatb.2006.06.005.
- [51] Y.-L. Fang, K. N. Heck, P. J. J. Alvarez, and M. S. Wong, “Kinetics Analysis of Palladium/Gold Nanoparticles as Colloidal Hydrodechlorination Catalysts,” *ACS Catal*, vol. 1, no. 2, pp. 128–138, 2011, doi: 10.1021/cs100067k.
- [52] S. Li, Y. L. Fang, C. D. Romanczuk, Z. Jin, T. Li, and M. S. Wong, “Establishing the trichloroethene dechlorination rates of palladium-based catalysts and iron-based reductants,” *Appl Catal B*, vol. 125, pp. 95–102, Aug. 2012, doi: 10.1016/j.apcatb.2012.05.025.
- [53] S. Ailawar *et al.*, “On the dual role of the reactant during aqueous phase hydrodechlorination of trichloroethylene (HDC of TCE) using Pd supported on swellable organically modified silica (SOMS),” *Appl Catal B*, vol. 291, Aug. 2021, doi: 10.1016/j.apcatb.2021.120060.
- [54] H. Sohn *et al.*, “Hydrodechlorination of trichloroethylene over Pd supported on swellable organically-modified silica (SOMS),” *Appl Catal B*, vol. 203, pp. 641–653, Apr. 2017, doi: 10.1016/j.apcatb.2016.10.032.
- [55] S. Ordóñez, B. P. Vivas, and F. V. Díez, “Minimization of the deactivation of palladium catalysts in the hydrodechlorination of trichloroethylene in

- wastewaters,” *Appl Catal B*, vol. 95, no. 3–4, pp. 288–296, Apr. 2010, doi: 10.1016/j.apcatb.2010.01.006.
- [56] D. L. Anderson, “Chemical Composition of the Mantle,” 1983.
- [57] X. Ma, Y. Liu, X. Li, J. Xu, G. Gu, and C. Xia, “Water: The most effective solvent for liquid-phase hydrodechlorination of chlorophenols over Raney Ni catalyst,” *Appl Catal B*, vol. 165, pp. 351–359, Apr. 2015, doi: 10.1016/j.apcatb.2014.10.035.
- [58] S. Zinovyev, A. Perosa, S. Yufit, and P. Tundo, “Hydrodechlorination and hydrogenation over Raney-Ni under multiphase conditions: Role of multiphase environment in reaction kinetics and selectivity,” *J Catal*, vol. 211, no. 2, pp. 347–354, 2002, doi: 10.1006/jcat.2002.3755.
- [59] Y. Wang, J. Wang, G. Fan, and F. Li, “Synthesis of a novel Ni/C catalyst derived from a composite precursor for hydrodechlorination,” *Catal Commun*, vol. 19, pp. 56–60, Mar. 2012, doi: 10.1016/j.catcom.2011.12.035.
- [60] Z. Dong, X. Le, C. Dong, W. Zhang, X. Li, and J. Ma, “Ni@Pd core-shell nanoparticles modified fibrous silica nanospheres as highly efficient and recoverable catalyst for reduction of 4-nitrophenol and hydrodechlorination of 4-chlorophenol,” *Appl Catal B*, vol. 162, pp. 372–380, 2015, doi: 10.1016/j.apcatb.2014.07.009.
- [61] K. A. Tarach *et al.*, “Nickel loaded zeolites FAU and MFI: Characterization and activity in water-phase hydrodehalogenation of TCE,” *Appl Catal A Gen*, vol. 568, pp. 64–75, Nov. 2018, doi: 10.1016/j.apcata.2018.09.026.
- [62] M. Martino, “Hydrodechlorination of dichloromethane, trichloroethane, trichloroethylene and tetrachloroethylene over a sulfided Ni/Mo- $\gamma$ -alumina catalyst,” *Appl Catal B*, vol. 20, no. 4, pp. 301–307, Apr. 1999, doi: 10.1016/S0926-3373(98)00120-9.

- [63] A. Śrębowata, R. Baran, G. Słowik, D. Lisovytskiy, and S. Dzwigaj, “Influence of the postsynthesis preparation procedure on catalytic behaviour of Ag-loaded BEA zeolites in the hydrodechlorination of 1,2-dichloroethane into value added products,” *Appl Catal B*, vol. 199, pp. 514–522, Dec. 2016, doi: 10.1016/j.apcatb.2016.06.060.
- [64] A. Śrębowata, R. Baran, D. Lisovytskiy, I. I. Kamińska, and S. Dzwigaj, “Catalytic conversion of trichloroethylene on nickel containing beta zeolites into value added products,” *Catal Commun*, vol. 57, pp. 107–110, Dec. 2014, doi: 10.1016/j.catcom.2014.08.023.
- [65] P. S. Chintawar and H. L. Greene, “Adsorption and catalytic destruction of trichloroethylene in hydrophobic zeolites,” 1997.
- [66] M. C. Silaghi, C. Chizallet, and P. Raybaud, “Challenges on molecular aspects of dealumination and desilication of zeolites,” *Microporous and Mesoporous Materials*, vol. 191. Elsevier, pp. 82–96, 2014. doi: 10.1016/j.micromeso.2014.02.040.
- [67] R. Giudici, H. W. Kouwenhoven, and R. Prins, “Comparison of nitric and oxalic acid in the dealumination of mordenite,” 2000.
- [68] S. K. Saxena, N. Viswanadham, and A. H. Al-Muhtaseb, “Enhanced selective oxidation of benzyl alcohol to benzaldehyde on mesopore created mordenite catalyst,” *Journal of Porous Materials*, vol. 23, no. 6, pp. 1671–1678, Dec. 2016, doi: 10.1007/s10934-016-0228-6.
- [69] Z. Qin *et al.*, “Defect-engineered zeolite porosity and accessibility,” *J Mater Chem A Mater*, vol. 8, no. 7, pp. 3621–3631, Feb. 2020, doi: 10.1039/c9ta11465c.
- [70] A. Al-Nayili, M. Albdiry, and N. Salman, “Dealumination of Zeolite Frameworks and Lewis Acid Catalyst Activation for Transfer Hydrogenation,” *Arab J Sci Eng*, vol. 46, no. 6, pp. 5709–5716, Jun. 2021, doi: 10.1007/s13369-020-05312-w.

- [71] S. Afzal *et al.*, “Controlling the rate of change of Ni dispersion in commercial catalyst by ALD overcoat during dry reforming of methane,” *Int J Hydrogen Energy*, vol. 45, no. 23, pp. 12835–12848, Apr. 2020, doi: 10.1016/j.ijhydene.2020.03.008.
- [72] J. Friedland, B. Kreitz, H. Grimm, T. Turek, and R. Güttel, “Measuring Adsorption Capacity of Supported Catalysts with a Novel Quasi-Continuous Pulse Chemisorption Method,” *ChemCatChem*, vol. 12, no. 17, pp. 4373–4386, Sep. 2020, doi: 10.1002/cctc.202000278.
- [73] S. Mintova, Alenka. Ristić, M. Rangus, and Nataša. Novak Tušar, *Verified syntheses of zeolitic materials*. Synthesis Commission of the International Zeolite Association, 2016.
- [74] Z. A. Alothman, “A review: Fundamental aspects of silicate mesoporous materials,” *Materials*, vol. 5, no. 12. pp. 2874–2902, 2012. doi: 10.3390/ma5122874.
- [75] M. Shamzhy, M. Opanasenko, P. Concepción, and A. Martínez, “New trends in tailoring active sites in zeolite-based catalysts,” *Chemical Society Reviews*, vol. 48, no. 4. Royal Society of Chemistry, pp. 1095–1149, Feb. 21, 2019. doi: 10.1039/c8cs00887f.
- [76] S. Narayanan, J. J. Vijaya, S. Sivasanker, M. Alam, P. Tamizhdurai, and L. J. Kennedy, “Characterization and catalytic reactivity of mordenite - Investigation of selective oxidation of benzyl alcohol,” *Polyhedron*, vol. 89, pp. 289–296, Mar. 2015, doi: 10.1016/j.poly.2014.12.038.
- [77] A. N. C. van laak, R. W. Gosselink, S. L. Sagala, J. D. Meeldijk, P. E. de Jongh, and K. P. de Jong, “Alkaline treatment on commercially available aluminum rich mordenite,” *Appl Catal A Gen*, vol. 382, no. 1, pp. 65–72, Jun. 2010, doi: 10.1016/j.apcata.2010.04.023.
- [78] G. Ertl, H. Knözinger, F. Schüth, and J. Weitkamp, *Handbook of heterogeneous catalysis*, 2nd ed., vol. 1. WILEY-VCH, 2008.

- [79] R. J. Gorte and S. P. Crossley, "A perspective on catalysis in solid acids," *Journal of Catalysis*, vol. 375. Academic Press Inc., pp. 524–530, Jul. 01, 2019. doi: 10.1016/j.jcat.2019.07.015.
- [80] K. Hadjiivanov, "Identification and Characterization of Surface Hydroxyl Groups by Infrared Spectroscopy," 2014, pp. 99–318. doi: 10.1016/B978-0-12-800127-1.00002-3.
- [81] X. F. Li, R. Prins, and J. A. van Bokhoven, "Synthesis and characterization of mesoporous mordenite," *J Catal*, vol. 262, no. 2, pp. 257–265, Mar. 2009, doi: 10.1016/j.jcat.2009.01.001.
- [82] M. Ravi, V. L. Sushkevich, and J. A. van Bokhoven, "On the location of Lewis acidic aluminum in zeolite mordenite and the role of framework-associated aluminum in mediating the switch between Brønsted and Lewis acidity," *Chem Sci*, vol. 12, no. 11, pp. 4094–4103, Mar. 2021, doi: 10.1039/d0sc06130a.
- [83] P. Castro-Fernández *et al.*, "Propane Dehydrogenation on Ga<sub>2</sub>O<sub>3</sub>-Based Catalysts: Contrasting Performance with Coordination Environment and Acidity of Surface Sites," *ACS Catal*, vol. 11, no. 2, pp. 907–924, Jan. 2021, doi: 10.1021/acscatal.0c05009.
- [84] G. Celik, S. A. Ailawar, S. Gunduz, P. L. Edmiston, and U. S. Ozkan, "Formation of carbonaceous deposits on Pd-based hydrodechlorination catalysts: Vibrational spectroscopy investigations over Pd/Al<sub>2</sub>O<sub>3</sub> and Pd/SOMS," *Catal Today*, vol. 323, pp. 129–140, Feb. 2019, doi: 10.1016/j.cattod.2018.05.001.
- [85] G. Eisenman, "Cation Selective Glass Electrodes and their Mode of Operation," *Biophys J*, vol. 2, no. 2, pp. 259–323, 1962, doi: 10.1016/S0006-3495(62)86959-8.
- [86] A. De Lucas, J. L. Valverde, F. Dorado, A. Romero, and I. Asencio, "Influence of the ion exchanged metal (Cu, Co, Ni and Mn) on the selective

- catalytic reduction of NO<sub>x</sub> over mordenite and ZSM-5,” *J Mol Catal A Chem*, vol. 225, no. 1, pp. 47–58, Jan. 2005, doi: 10.1016/j.molcata.2004.08.036.
- [87] J. F. Da Costa-Serra, M. T. Navarro, F. Rey, and A. Chica, “Bioethanol steam reforming on Ni-based modified mordenite. Effect of mesoporosity, acid sites and alkaline metals,” in *International Journal of Hydrogen Energy*, Apr. 2012, pp. 7101–7108. doi: 10.1016/j.ijhydene.2011.10.086.
- [88] B. Pawelec, R. Mariscal, R. M. Navarro, J. M. Campos-Martin, and J. L. G. Fierro, “Simultaneous 1-pentene hydroisomerisation and thiophene hydrodesulphurisation over sulphided Ni/FAU and Ni/ZSM-5 catalysts,” *Appl Catal A Gen*, vol. 262, no. 2, pp. 155–166, May 2004, doi: 10.1016/j.apcata.2003.11.037.
- [89] J. Shan *et al.*, “Conversion of methane to methanol with a bent mono( $\mu$ -oxo)dinickel anchored on the internal surfaces of micropores,” *Langmuir*, vol. 30, no. 28, pp. 8558–8569, Jul. 2014, doi: 10.1021/la501184b.
- [90] G. Zhao, E. Benhelal, A. Adesina, E. Kennedy, and M. Stockenhuber, “Comparison of Direct, Selective Oxidation of Methane by N<sub>2</sub>O over Fe-ZSM-5, Fe-Beta, and Fe-FER Catalysts,” *Journal of Physical Chemistry C*, vol. 123, no. 45, pp. 27436–27447, Nov. 2019, doi: 10.1021/acs.jpcc.9b04388.
- [91] N. Kosinov, C. Liu, E. J. M. Hensen, and E. A. Pidko, “Engineering of Transition Metal Catalysts Confined in Zeolites,” *Chemistry of Materials*, vol. 30, no. 10. American Chemical Society, pp. 3177–3198, May 22, 2018. doi: 10.1021/acs.chemmater.8b01311.
- [92] Y. Chai *et al.*, “Noble Metal Particles Confined in Zeolites: Synthesis, Characterization, and Applications,” *Advanced Science*, vol. 6, no. 16. John Wiley and Sons Inc, Aug. 01, 2019. doi: 10.1002/advs.201900299.

- [93] N. M. Phadke, J. Van Der Mynsbrugge, E. Mansoor, A. B. Getsoian, M. Head-Gordon, and A. T. Bell, "Characterization of Isolated Ga<sup>3+</sup> Cations in Ga/H-MFI Prepared by Vapor-Phase Exchange of H-MFI Zeolite with GaCl<sub>3</sub>," *ACS Catal*, vol. 8, no. 7, pp. 6106–6126, Jul. 2018, doi: 10.1021/acscatal.8b01254.
- [94] T. Otto, S. I. Zones, and E. Iglesia, "Challenges and strategies in the encapsulation and stabilization of monodisperse Au clusters within zeolites," *J Catal*, vol. 339, pp. 195–208, Jul. 2016, doi: 10.1016/j.jcat.2016.04.015.
- [95] B. M. McD BAKER and E. K. Rideal, "THE ADSORPTION OF CARBON MONOXIDE BY NICKEL."
- [96] J. T. Yates and C. W. Garland, "INFRARED STUDIES OF CARBON MONOXIDE CHEMISORBED ON NICKEL AND ON MERCURY-POISONED NICKEL SURFACES," 1960.
- [97] V. M. Gonzalez-Delacruz, R. Pereñíguez, F. Ternero, J. P. Holgado, and A. Caballero, "Modifying the size of nickel metallic particles by H<sub>2</sub>/CO Treatment in Ni/ZrO<sub>2</sub> methane dry reforming catalysts," *ACS Catal*, vol. 1, no. 2, pp. 82–88, Feb. 2011, doi: 10.1021/cs100116m.
- [98] T. Weidlich, "Applicability of nickel-based catalytic systems for hydrodehalogenation of recalcitrant halogenated aromatic compounds," *Catalysts*, vol. 11, no. 12. MDPI, Dec. 01, 2021. doi: 10.3390/catal11121465.
- [99] B. Schrick, J. L. Blough, A. D. Jones, and T. E. Mallouk, "Hydrodechlorination of trichloroethylene to hydrocarbons using bimetallic nickel-iron nanoparticles," *Chemistry of Materials*, vol. 14, no. 12, pp. 5140–5147, Dec. 2002, doi: 10.1021/cm020737i.
- [100] E. Güvenç and M. G. Ahunbay, "Adsorption of methyl tertiary butyl ether and trichloroethylene in MFI-type zeolites," *Journal of Physical Chemistry C*, vol. 116, no. 41, pp. 21836–21843, Oct. 2012, doi: 10.1021/jp3067052.

- [101] L. Intriago, E. Díaz, S. Ordóñez, and A. Vega, "Combustion of trichloroethylene and dichloromethane over protonic zeolites: Influence of adsorption properties on the catalytic performance," *Microporous and Mesoporous Materials*, vol. 91, no. 1–3, pp. 161–169, Apr. 2006, doi: 10.1016/j.micromeso.2005.11.043.
- [102] Y. H. Choi and W. Y. Lee, "Effect of Ni loading and calcination temperature on catalyst performance and catalyst deactivation of Ni/SiO<sub>2</sub> in the hydrodechlorination of 1,2-dichloropropane into propylene," 2000.
- [103] J. F. Moulder, W. F. Stickle, P. E. Sobol, K. D. Bomben, and J. Chastain, "Handbook of X-ray Photoelectron Spectroscopy A Reference Book of Standard Spectra for Identification and Interpretation of XPS Data."

## APPENDICES

### A. Calculations of Catalytic Activity Parameters

In this thesis study, measure of the catalytic activity was shown by conversion of TCE.

TCE conversion at any time was calculated according to difference between the initial TCE concentration and TCE concentration at the measured time intervals as described in chapter 4.3.

$$X_{TCE}(t) = \frac{C_{TCE,0} - C_{TCE}(t)}{C_{TCE,0}} \quad \text{Eqn.A1}$$

Selectivity of each product was calculated according to equation A2. Selectivity was described as the ratio specific product concentration to sum of all product concentrations. TCE is not included to calculation as product.

$$S_i = 100 \times \frac{C_{i,t}}{\sum_n C_n} \quad \text{Eqn.A2}$$

Gas hourly space velocity (GHSV) was calculated according to equation A3. For all 3 samples, bed height was approximately measured as 0.45 cm. Diameter of the reactor bed was also 0.45 cm for HDC activity tests.

$$\begin{aligned} GHSV &= \frac{\text{volumetric flow rate of the reactants}}{\text{volume of the reactor bed}} \quad \text{Eqn.A3} \\ &= \frac{\frac{30 \text{ cm}^3}{\text{min}} \times \frac{60 \text{ min}}{1 \text{ hour}}}{\pi \times \left(\frac{0.45 \text{ cm}}{2}\right)^2 \times 0.45 \text{ cm}} \cong 25160 \text{ h}^{-1} \end{aligned}$$

TCE percentage in the reactor feedstock was calculated according to Raoult's Law. Raoult's law states that the partial pressure of every compound of an ideal mixture of liquid is equal to vapor pressure of the pure component in the liquid phase. Total pressure above the solution is equal to the fractional sum of vapor pressure of each liquid in the solution. Following equation describes the Raoult's law:

$$P = P_A^{vap} \cdot x_A + P_B^{vap} \cdot x_B \quad \text{Eqn. A4}$$

For a pure substance Eqn. A4 transformed into following Equation.

$$P = P_A^{vap} \quad \text{for } x_A=1 \text{ and } x_B=0.$$

To find vapor pressure Antoine equation was used.

$$\log_{10} P^{vap} = A - \frac{B}{C+T} \quad P^{vap} \text{ is in bar, T is in K} \quad \text{Eqn. A5}$$

Antoine constants for TCE are  $A=3.55346$     $B = 974.538$     $C= -85.811$

In the bubbler there is a constant flow of argon flowing under constant pressure of 1 atm. For 5 sccm of Ar flow through a TCE bubbler at 27°C, flow of TCE was found as follows.

$$Q_{TCE} = \frac{5 \text{ cm}^3}{\text{min}} \times 10^{(3.55346 - \frac{974.538}{300 - 85.811})} \times \frac{1}{1.01325 \text{ bar}} = \frac{0.414 \text{ cm}^3}{\text{min}}$$

$$\frac{Q_{H_2}}{Q_{TCE}} = \frac{25 \text{ sccm}}{0.414 \text{ sccm}} = 60.4$$

## B. Result of CO pulse chemisorption on Ni-HMOR

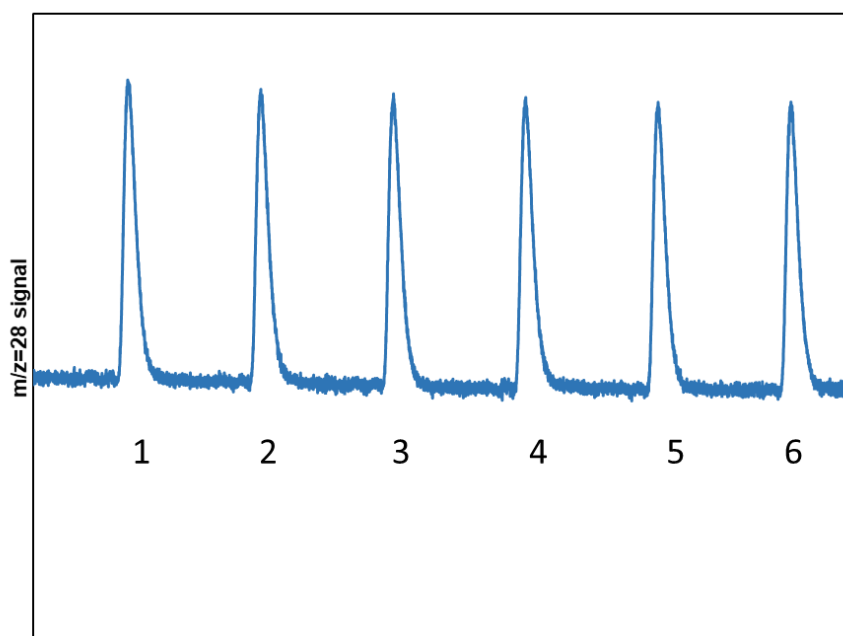


Figure 31. m/z=28 signal collected for 6 CO pulses on the Ni-HMOR sample.

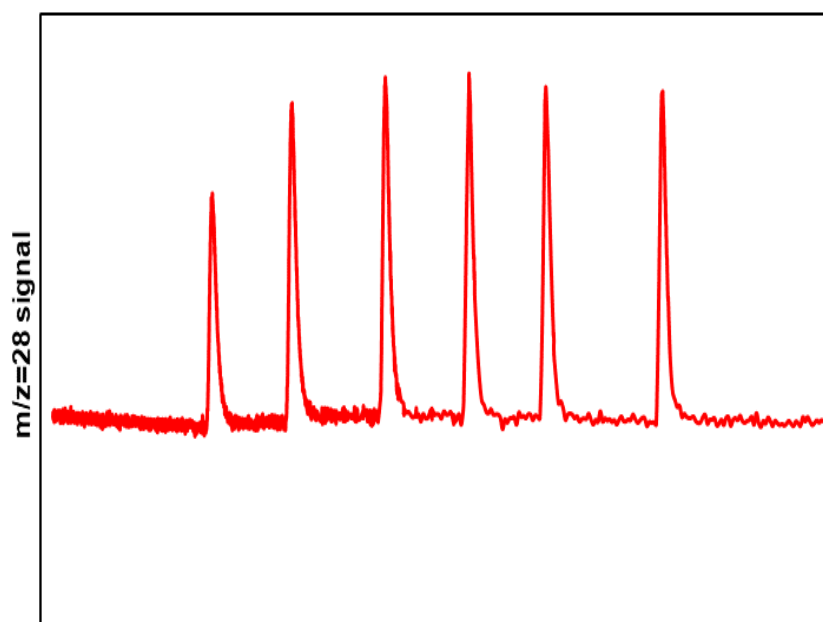


Figure 32. m/z=28 signal collected for 6 CO pulses on the Pt/TiO<sub>2</sub> sample.

### C. XPS Results of HDC Used Ni-HMOR catalyst

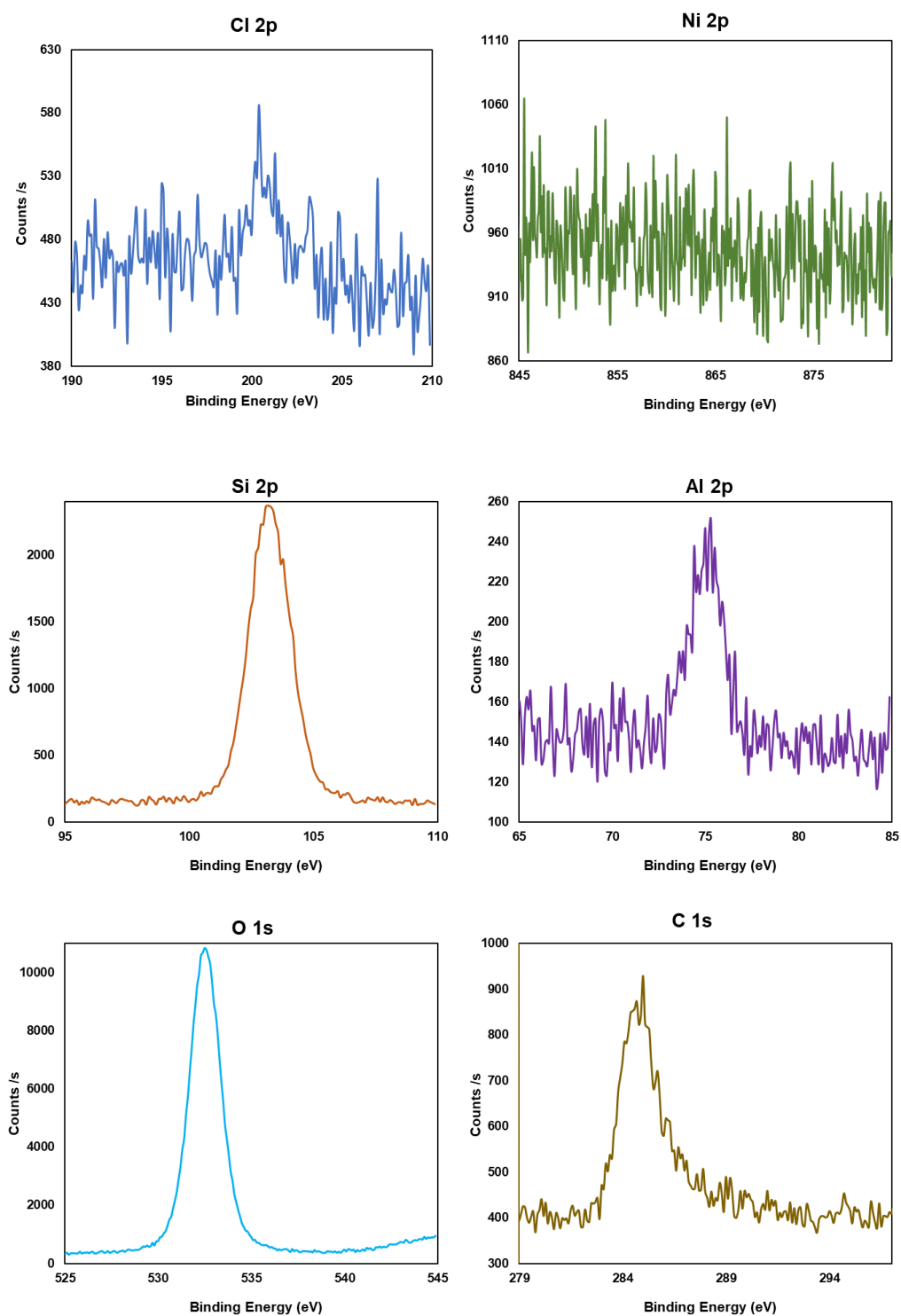


Figure 33 Elemental XPS results of HDC used Ni -HMOR catalyst.

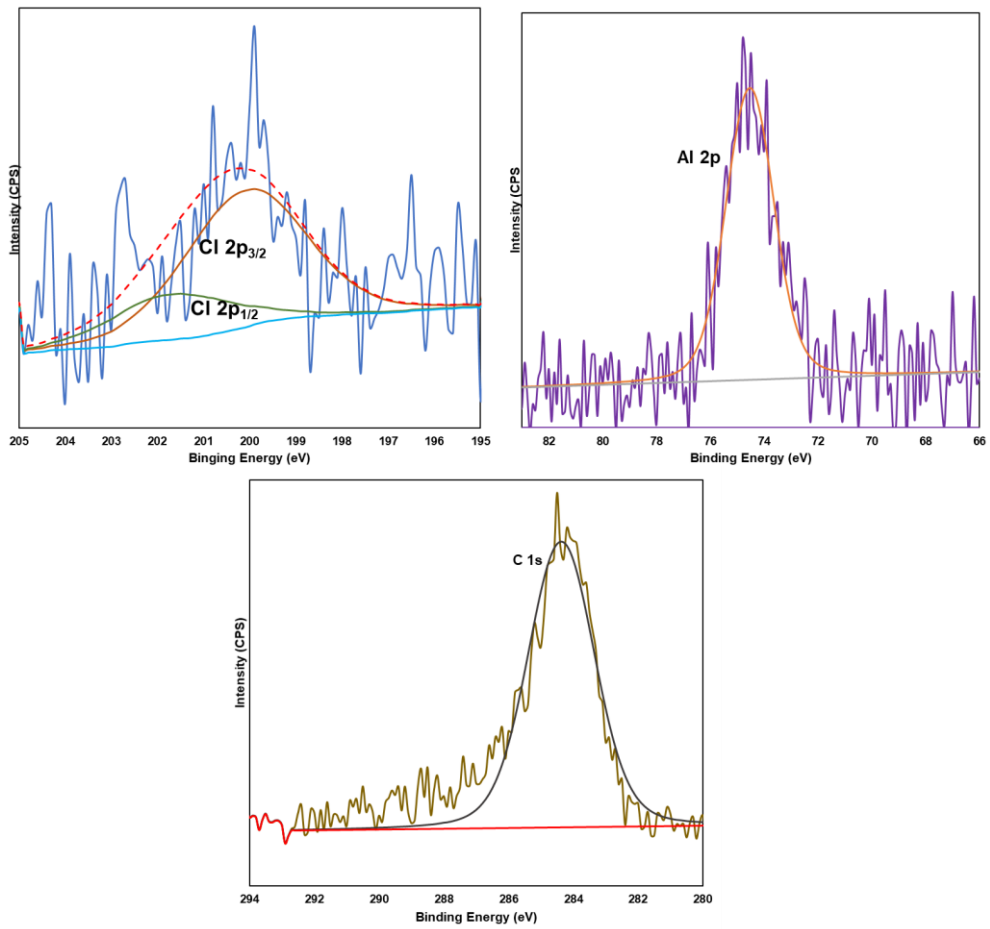


Figure 34. Deconvoluted XPS plots for Cl, Al, and C elements on HDC used Ni-HMOR catalyst.

#### D. XRD Results of Ni exchanged XMHMORs

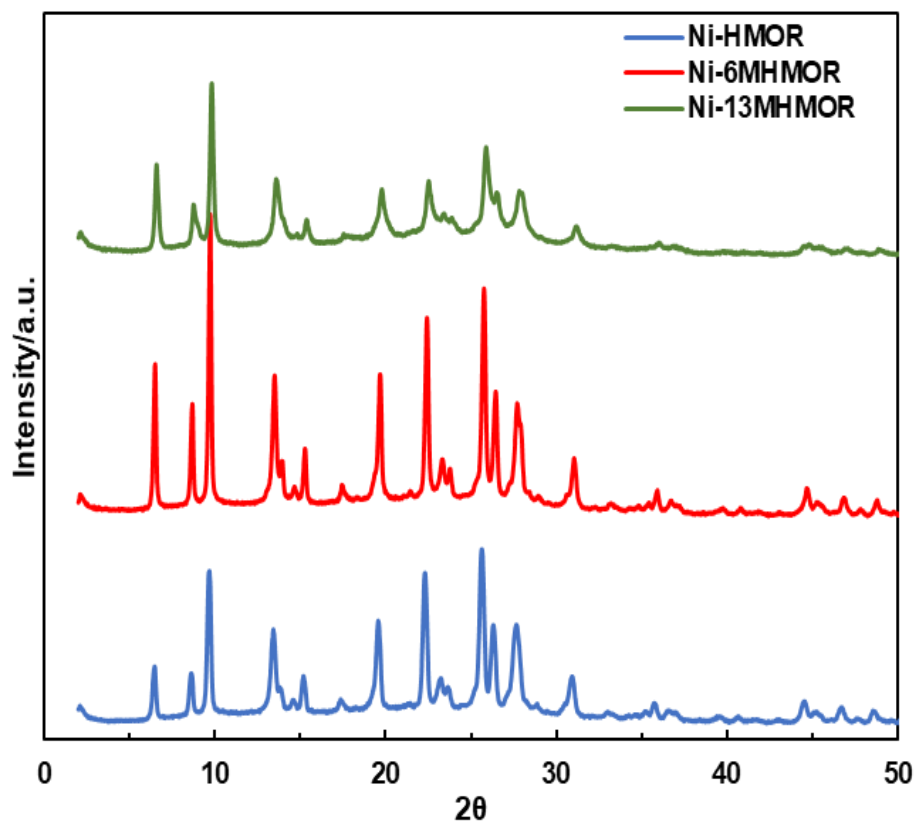


Figure 35. XRD patterns obtained for Ni exchanged bare and dealuminated MORs.